THERMAL AND NON-THERMAL PROCESSES INVOLVING WATER ON APOLLO LUNAR SAMPLES AND METAL OXIDE POWDERS

A Dissertation
Presented to
The Academic Faculty

by

Michael Joseph Poston

In Partial Fulfillment
of the Requirements for the Degree
Doctor of Philosophy in the
School of Chemistry and Biochemistry

Georgia Institute of Technology

August 2014

THERMAL AND NON-THERMAL PROCESSES INVOLVING WATER ON APOLLO LUNAR SAMPLES AND METAL OXIDE POWDERS

Approved by:

Dr. Thomas Orlando, Advisor
School of Chemistry and Biochemistry
Georgia Institute of Technology

Dr. Z. John Zhang
School of Chemistry and Biochemistry
Georgia Institute of Technology

Dr. Angus Wilkinson
School of Chemistry and Biochemistry
Georgia Institute of Technology

Dr. David Sherrill
School of Chemistry and Biochemistry
Georgia Institute of Technology

Dr. Britney Schmidt
School of Earth and Atmospheric Sciences
Georgia Institute of Technology

Date Approved: April 16, 2014

Acknowledgements

There are a number of people who have contributed to my success in graduate school. First, I'd like to thank my PhD advisor, Prof. Thomas Orlando, for support, valuable critiques on ideas and manuscripts, and for always amazingly coming through just in the nick of time when it really mattered. Maria Rusert, my partner, for her understanding and encouragement and for generally being awesome. Drs. Alexandr Aleksandrov, Gregory Grieves, Chris Bennett, Jason MacLain, Reuben Gann, Claire Pirim, Michele Dawley, Denis Sokolov, Alice DeSimone, and former and present students Hannah Barks, Josh Symonds, and the rest of the Orlando group (past and present), as well as former Georgia Tech student Will Underwood, for significant assistance with maintenance and repair of equipment, gathering and evaluation of data, and making pesky software programs perform as desired. Georgia Tech Chemistry Professors Angus Wilkinson, David Sherrill, Z. John Zhang, and Andrew Lyon all contributed significantly to my growth as a scientist and Dr. Cameron Tyson guided me through of a number of tricky situations with Georgia Tech.

I would not have discovered my love for planetary science if not for collaborators Dr. Charles Hibbitts and Prof. M. Darby Dyar drawing me into the field in the first place or the perspective imparted by Professors Carol Paty, James Wray, and Britney Schmidt on just how amazing our solar system is. Thinking further back, my former co-workers: Dr. Jeff Kenvin, Tony Thornton, and Greg Thiele, my undergraduate professors: Kerry Kuehn, Daniel Ebeling, Keith Beyer, and Kevin Glaeske, and my high school chemistry

teacher: Mr. Tracey all played significant roles in my development into the scientist I am today. And last, but definitely not least, I'd like to thank my parents and family for support beyond description through the first 21 years of my life, and continued encouragement and curiosity to this day.

Table of Contents

List of Tables

List of Figures

Summary

Water is of interest for understanding the formation history and habitability of past and present solar system environments. It also has potential as a resource - when split to its constituent oxygen and hydrogen - both in space and on the Earth. Determining the sources, evolution, and eventual fate of water on bodies easily reachable from Earth, especially Earth's moon, is thus of high scientific and exploration value to the private sector and government space agencies. Understanding how to efficiently split water with solar energy has potential to launch a hydrogen economy here on Earth and to power spacecraft more sustainably to far away destinations. To address the fundamental interactions of water with important surfaces relevant to space exploration and technology development, temperature programmed desorption (TPD) and water photolysis experiments under well controlled adsorbate coverages have been carried out and are described in detail in this thesis.

TPD experiments under ultra-high vacuum (UHV) conditions were conducted on lunar surrogate materials and genuine lunar samples brought to Earth by the Apollo program. The TPD's were conducted to determine the desorption activation energies of water chemisorbed directly to the powder surfaces, knowledge of which can improve existing models of water evolution on Earth's moon and aid in interpreting data collected by spacecraft-based investigations at the Moon.

The TPD experiments of molecular water interacting with two lunar surrogates (micronized JSC-1A and albite) in ultra-high vacuum revealed water desorption during

initial heating to 750 K under ultra-high vacuum. Diffuse Reflectance Infrared Fourier Transform Spectroscopy (DRIFTS) indicated possible water formation during the initial heating via recombinative desorption of native hydroxyls above 425 $\pm$ 25K. Dissociative chemisorption of water (i.e., formation of surface hydroxyl sites) was not observed on laboratory time scales after controlled dosing of samples (initially heated above 750 K) with 0.2 – 500 L exposures of water. However, pre-heated samples of both types of surrogates were found to have a distribution of molecular water chemisorption sites, with albite having at least twice as many as the JSC-1A samples by mass. A fit to the TPD data yields a distribution function of desorption activation energies ranging from ~0.45 eV to 1.2 eV. Using the fitted distribution function as an initial condition, the TPD process was simulated on the timescale of a lunation. A preview of these results and their context was published in *Icarus* (2011) 213, 64, doi: 10.1016/j.icarus.2011.02.015 by lead author Charles Hibbitts and the full treatment of the results from the TPD on lunar surrogates (presented here in Chapter 2) has been published in the *Journal of Geophysical Research – Planets* (2013) 118, 105, doi: 10.1002/jgre.20025 by lead author Michael J Poston.

The desorption activation energies for water molecules chemisorbed to Apollo lunar samples 72501 and 12001 were determined by temperature programmed desorption (TPD) experiments in ultra-high vacuum. A significant difference in both the energies and abundance of chemisorption sites was observed, with 72501 retaining up to 40 times more water (by mass) and with much stronger interactions, possibly approaching 1.5 eV. The dramatic difference between the samples may be due to differences in

mineralogy, surface exposure age, and contamination of sample 12001 with oxygen and water vapor before it arrived at the lunar sample storage facility. The distribution function of water desorption activation energies for sample 72501 was used as an initial condition to mathematically simulate a TPD experiment with the temperature program matching the lunar day. The full treatment of the TPD results from these two lunar samples (presented here in Chapter 3) has been submitted with the title "Water chemisorption interactions with Apollo lunar samples 72501 and 12001 by ultra-high vacuum temperature programmed desorption experiments" to *Icarus* for publication in the special issue on lunar volatiles by lead author Michael J Poston.

A new ultra-high vacuum system (described in Chapter 4) was designed and constructed for planned experiments examining the possible formation of hydrated species, including water, from interaction of solar wind hydrogen with oxygen in the lunar regolith and to examine the effects of the active radiation environment on water adsorption and desorption behavior on lunar materials. This system has been designed in close collaboration with Dr. Chris J Bennett.

An examination of a unique system for water photolysis - zirconia nanoparticles for hydrogen production from water with ultra-violet photons - was performed to better understand the mechanism and efficiency of water splitting on this catalyst. Specifically, formation of H_2 from photolysis of water adsorbed on zirconia (ZrO_2) nanoparticles using 254 nm (4.9 eV) and 185 nm (6.7 eV) photon irradiation was examined. The H_2 yield was approximately an order of magnitude higher using monoclinic versus cubic phase nanoparticles. For monoclinic particles containing 2 monolayers (ML) of water,

the maximum H_2 production rate was ~0.4 μmole hr^{-1} m^{-2} using 185 + 254 nm excitation and a factor of 10 lower using only 254 nm. UV reflectance reveals that monoclinic nanoparticles contain fewer defects than cubic nanoparticles. A H_2O coverage dependence study of the H_2 yield is best fit by a sum of interactions involving at least two types of adsorbate-surface complexes. The first dominates up to ~0.06 ML and is attributed to H_2O chemisorbed at surface defect sites. The second dominates at coverages up to a bilayer. H_2 formation is maximum within this bilayer and likely results from efficient energy transfer from the particle to the interface. Energy transfer is more efficient for the monoclinic ZrO_2 nanoparticles and likely involves mobile excitons. These results (presented in Chapter 5) have been submitted with the title "UV Photon-Induced Water Decomposition on Zirconia Nanoparticles" for publication in the *Journal of Physical Chemistry C* by lead author Michael J Poston. This paper has been reviewed and will be accepted after minor modification.

Introduction

Water is the perhaps the most important molecule in the solar system. Here on Earth, water is necessary for sustaining all known life. NASA has taken a strategy of 'following the water' in searching for locations of past or present habitability in the Universe. Deposits of water, and the isotopic ratios of atoms in those deposits, carry information about the history of a body, which can potentially be informative with regard to the formation and history of the solar system. Water on solar system bodies near Earth is also of interest for in situ resource utilization (ISRU). The above items lead to significant interest in the community for understanding the sources, dynamics, and fate of any water that is or ever has been on Earth's moon. There is interest and commercial value in using solar irradiation to split water into hydrogen and oxygen fuels, effectively storing the solar energy to be reacted at will back into water as an energy source that releases no greenhouse gases.

1.1 The Types and Locations of Hydration on Earth's Moon

Water is simply two hydrogen atoms bonded to one oxygen atom, but in geology any form of hydration can yield information about the presence or history of water. Hydration can appear on the Moon in three broad varieties: 1) deep, ancient hydrogen from the lunar interior incorporated as hydroxyl or structural water in minerals that have erupted to the surface in ancient magmatic flows, 2) cold-trapped water and hydrogen of ancient and/or modern origin cold-trapped in permanently shadowed regions (PSRs) at the lunar poles and possibly at lower latitudes below the thermal skin

depth, and 3) surfacial hydrogen from solar wind implantation seen as H, SiH, SiOH, H_2, and possibly H_2O. Each of these reservoirs of hydration can have limited exchange with the others via diffusion and migration promoted by thermal cycling, radiation-induced desorption, and impact events.

Evidence for each of these types of hydration has been found through investigation of the Moon using orbiting spacecraft and by collecting samples to be examined with state-of-the-art instrumentation back on Earth. Ancient hydration, possibly trapped in minerals since the initial formation of the Moon, has been liberated from deep within magmatic lunar glass beads from ancient eruptions and from apatite (a mineral where water would have been concentrated during the crystallization magma) by ion microprobe investigations [*Saal et al.*, 2008; *Greenwood et al.*, 2011a; *Greenwood et al.*, 2011b; *Liu et al.*, 2012; *Hui et al.*, 2013]. Surfacial hydrogen has also been detected in lunar samples by a resonant nuclear reaction between ^{19}F and $^{1}H^{16}O$ in the first 250 nm of lunar rocks and glass beads [*Leich et al.*, 1973]. Spacecraft-based investigations also showed evidence of surfacial hydrogen, with three independent observations finding absorption bands near 3 μm in reflected sunlight that are consistent with mineral-bound hydroxyl and possibly water within the first few micrometers of lunar surface materials [*Clark*, 2009; *Pieters et al.*, 2009; *Sunshine et al.*, 2009]. Results consistent with polar hydration have been returned from several instruments aboard NASA's Lunar Reconnaissance Orbiter (LRO), but a self-consistent story of where the hydration is located and in what form has not yet been arrived upon by the community. (Conversely, self-consistent evidence for macroscopic water-ice deposits has been seen at PSR's on

the planet Mercury using the same set of techniques [*Harmon and Slade*, 1992; *Lawrence et al.*, 2013; *Neumann et al.*, 2013; *Paige et al.*, 2013].) Polar hydration was observed, however, in the Cabeus crater PSR on the Moon in the form of water-ice particles, water molecules, hydroxyl, hydrogen molecules, and atomic hydrogen in the ejecta plume from the Lunar CRater Observation and Sensing Satellite (LCROSS) impact experiment [*Colaprete et al.*, 2010; *Gladstone et al.*, 2010].

The form and distribution of hydration on the Moon is a dynamic process of past and current interest to the community. Up until *Saal et al.* [2008] work, the equatorial lunar samples collected by the Apollo program were believed to contain only hydrogen implanted from the solar wind and no primordial hydration. In addition to Saal et al's work, recent observations with spacecraft-based instrumentation have shown spectral signatures at 2.95 μm in the infrared consistent with (but not unique to) molecular water interacting with minerals at high lunar latitudes [*Clark*, 2009; *Pieters et al.*, 2009; *Sunshine et al.*, 2009]. These observations also showed a diurnal variation in band depth, with the greatest band depth near the morning terminator, consistent with water constantly migrating away from the warmth-bringing sunlight [*Clark*, 2009; *Sunshine et al.*, 2009]. There is also a hint of increased hydrogen concentration near the morning terminator as seen by neutron depletion counting from orbit, which may indicate migrating water near the terminator [*Livengood et al.*, 2014]. Each of these possible detections has significant unanswered questions and each is ambiguous regarding the assumptions and fundamental phenomenon that could lead to the

possible detections. Planetary scientists are turning to models of water behavior on the Moon in hopes of answering some of these questions.

Watson et al. [1961] first modeled the likelihood of water finding its way to lunar PSR cold traps, *Arnold* [1979] revisited the topic twenty years later and added in the possibility of water produced from implanted solar wind hydrogen combined with oxygen in the lunar regolith during micrometeoroid impacts, *Crider and Vondrak* [2000] updated the field for new understanding around the turn of the century with their own models that track what percentage of water from a given latitude would be expected to find its way to PSR's, and researchers today continue applying similar modeling techniques to simulate water movement both on the surface of the Moon and vertically in the porous regolith of the Moon, Vesta, and asteroids (eg. [*Grieves et al.*, 2010; *Hurley*, 2010]). These models use a key simplification: they assume that individual water molecules interact with regolith grains with energetics similar to water molecules on ice. This simplification ignores the likelihood of chemisorption – the (often) reversible formation of weak chemical bonds between an adsorbate molecule and the adsorbent substrate. In fact, at the low water abundances relevant on the Moon, regolith grains should have significantly less than a full monolayer of adsorbed water, and the direct interactions between the water molecules and the grains will dominate surface residence times on migrating molecules.

1.2 Water Adsorption Basics

Water adsorption has been studied extensively for metals and metal oxide powders [*Thiel and Madey*, 1987; *Henderson*, 2002]. Adsorption of water can be divided into

three general types - physisorption, molecular chemisorption, and dissociative chemisorption as hydroxyl – all of which have different structure on the surface but desorb as molecular water. The temperature of desorption and trends in the shape and temperature of desorption peaks when heating at a constant rate of temperature in time during temperature programmed desorption (TPD) experiments can carry information about the surface form of adsorbed water. Desorption is governed by the Polanyi-Wigner equation:

$$\frac{dN}{dt} = -kN^n, \tag{1.1}$$

where *N* is concentration (or coverage), *t* is time, *n* is the order of desorption, and *dN/dt* the rate of desorption. The rate constant, *k*, comes from the Arrhenius equation:

$$k = Ae^{-E_d / k_B T} \tag{1.2}$$

and is a function of temperature, T (in Kelvin), the desorption activation energy, E_d (in eV), and a pre-exponential factor, A, which has to do with how often the species tries to escape the surface; k_B is the Boltzmann constant. The key mathematical difference among the three surface forms of adsorbed water is that each has a different value for n: 0, 1, or 2 for physisorption, molecular chemisorption, and recombinative desorption (the term for desorption of water that had dissociatively adsorbed), respectively.

Theoretical desorption curves have been generated from the Polanyi-Wigner equation to demonstrate idealized desorption for each of the three surface forms of adsorbed water and are shown in Figure 1.1. Each color represents a set of desorption simulations with increasing initial water coverage. Physisorption uses desorption of

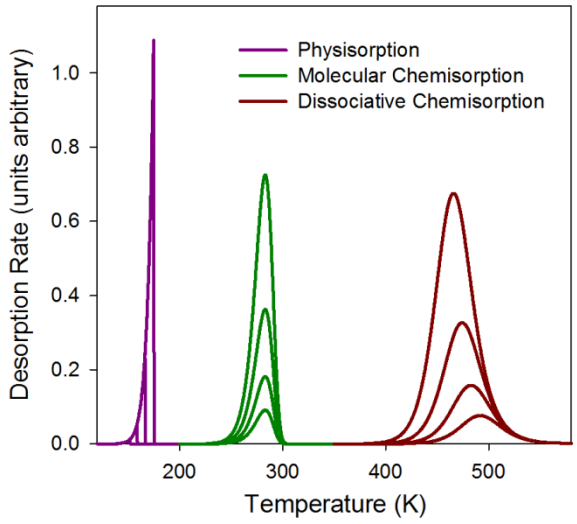

Figure 1.1: Simulated desorption curves for the three main categories of adsorbed water showing trends with increasing water coverage.

order zero and is indicated by a constant temperature for onset of desorption, an increasing temperature for peak maximum, and an increasing temperature for return to baseline. Molecular chemisorption uses desorption of order one and is indicated by a slightly decreasing temperature for onset of desorption, a constant temperature of peak maximum, and a slightly increasing temperature of return to baseline. Recombinative desorption uses desorption of order two and is indicated by decreasing temperature for onset of desorption, decreasing temperature for peak maximum, and constant temperature for return to baseline. The desorption activation energy for each curve was chosen to be typical of each process. Physisorption involves Van der Waals forces and requires the lowest energy to desorb, typically below 0.5 eV per molecule. Molecular chemisorption involves weak covalent interactions between the adsorbent and adsorbate, requiring greater energy to desorb. Dissociative adsorption actually changes

the bonding structure of the adsorbate, requiring the most energy to reverse, often 1 eV or more. Some dissociative adsorption is reversible, and other times the surface is oxidized, keeping the oxygen atom and releasing H_2 gas.

Molecular chemisorption of water typically involves the oxygen lone pairs. In the case of adsorption on metal-oxides, the results of photo-emission studies tend towards stabilization of the non-bonding $3a_1$ level [*Henderson*, 2002], resulting in an orientation with the oxygen down and the hydrogen atoms normal to the surface. Water will preferentially adsorb at locations of electron deficiency, such as cation sites and especially surface defects. Rather than form a 'bi-layer' as water tends to do on ordered metal surfaces, on metal-oxides water tends to build up by clustering around already adsorbed water molecules by hydrogen bonding.

The most important factor in whether water will dissociate upon adsorption is the surface structure, specifically the availability of a cation site for the water's oxygen atom to adsorb to and with a nearby oxygen atom to bond with one of the hydrogen atoms [*Henderson*, 2002]. It was mentioned above that recombinative desorption of hydroxyl groups as water should desorb with shape corresponding to order n=2, however, there are cases (eg. "geminal" and "vicinal") where two hydroxyl groups remain associated with each other on the surface and can exhibit desorption that appears to be of order n=0 or 1 [*D'Souza and Pantano*, 2002]. Numerous metal-oxide surfaces have been characterized for water dissociative adsorption and many will dissociate water at regular surface sites, many others are only active for dissociation when the surface is populated with defect sites, and still others show no water dissociation behavior at all.

Most surface science studies are performed on the simplest, most ordered surfaces obtainable, usually single crystals of meticulously cleaved and sputter-cleaned pure materials. Moving from a single crystal to an amorphous slab has been shown to significantly broaden desorption peaks (eg. Figure 1.2 [*Vidali and Li*, 2010]); moving to a powder broadens desorption peaks even further. The surfaces of lunar materials are anything but pure and ordered single crystals. On the contrary, lunar materials are constantly bombarded by 'space weathering' agents: micrometeoroids, cosmic rays, and ions, electrons, and ionizing radiation from the solar wind. Space weathering produces fractal-like surfaces with high defect concentrations, which may make them highly adsorbing of water. Chapters 2 and 3 describe TPD experiments examining the

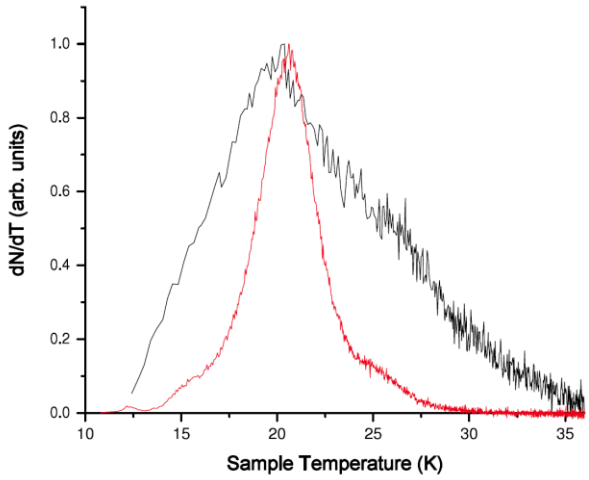

Figure 1.2: Example of the difference in shape of H_2 desorption peaks between a single crystal and an amorphous silicate. Taken from *Vidali and Li* [2010],

adsorption behavior of water on lunar materials and Chapter 4 describes a new ultra-high vacuum system designed and constructed to test solar-wind space weathering processes: the non-thermal reactions that can occur under solar wind exposure and the effects of these weathering processes on water adsorption behavior.

1.3 Water Photolysis on Zirconia Nanoparticles

In addition to thermal behavior of water on surfaces, there are non-thermal processes involving ions, electrons, and photons. Of particular interest is the catalytic decomposition of water on metal-oxide surfaces to effective store energy from solar-photon irradiation to produce hydrogen gas. One unique system for water photolysis is zirconia, which is one of very few materials to catalyze water decomposition without a metallic co-catalyst [*Sayama and Arakawa*, 1996; *Kudo and Miseki*, 2009]. Study of this system provides an opportunity to examine photolysis of adsorbed water at a basic level. Chapter 5 describes investigations of the water photolysis mechanism for this unique system.

CHAPTER 2

Measurement of Water Desorption Activation Energies From Lunar Surrogates

2.1 Introduction

The existence of reservoirs of water-ice in the permanently-shadowed regions of the lunar poles was first predicted by *Watson et al.* [1961]. The recent LCROSS (Lunar Crater Observation and Sensing Satellite) impact experiment at Cabeus crater confirmed the presence of up to 6% concentration (by mass) of water and ice in the ejecta plume [*Colaprete et al.*, 2010], yet the original source of this water is unknown. Three independent spacecraft observations also reported the presence of water and/or hydroxyl (OH) on the sunlit lunar surface [*Clark*, 2009; *Pieters et al.*, 2009; *Sunshine et al.*, 2009] based on interpretation of ~ 3-µm band reflectance measurements. The 3-µm band observations were poorly correlated with interpretations of neutron remote sensing data [*Pieters et al.*, 2009], however, reanalysis with new models shows promise for resolving the differences [*Lawrence et al.*, 2011].

Water has been measured in/on samples from the Apollo missions [e.g. *Gibson and Johnson* [1971] and refs. therein]. Based on isotopic analysis, it was concluded that all water removed from returned lunar samples resulted from terrestrial contamination [e.g. *Epstein and Taylor* [1974] and refs. therein]. Work by *Taylor et al.* [1995] used Fourier transform infrared (FTIR) spectroscopy to conclude that any OH- present in lunar

samples was at concentrations below detection limits, ca. 50 ppm. However, recent analyses of lunar picritic glass [*Saal et al.*, 2008] and lunar apatite [*Boyce et al.*, 2010; *Greenwood et al.*, 2011a] using advanced Secondary Ion Mass Spectrometry (SIMS) techniques reveal internal water (possibly in the form of hydroxyl groups) at concentrations up to 6050 ppm [*Greenwood et al.*, 2011b]. Isotopic ratios from these recent measurements span the range from enriched in ΔD (consistent with a cometary source) to depleted in ΔD (consistent with solar wind origin) [*Greenwood et al.*, 2011a]. *Crider and Vondrak* [2000] point out that water migration tends to artificially increase ΔD because lighter molecules are more likely to escape during transport.

Beyond the fundamental scientific and intellectual value of understanding the presence or absence of water on the Moon, water is an important resource for human exploration of the solar system. Availability of water may be the deciding factor in selecting targets for future human space exploration and the ability to predict locations of accessible water (and/or hydroxyls) will be valuable for space agencies worldwide. Many studies have modeled the stability and transport of water on the Moon (e.g. [*Watson et al.*, 1961; *Vasavada et al.*, 1999; *Hodges*, 2002; *Grieves et al.*, 2010; *Hurley*, 2010; *Ong et al.*, 2010; *Hibbitts* et al., 2011; *Siegler et al.*, 2011]). Several recent reviews discuss the known physical processes relevant to the production and retention of water and hydroxyl on the Moon [*Lucey et al.*, 2006; *Lucey*, 2009; *Dyar et al.*, 2010; *Hibbitts et al.*, 2011; *McCord et al.*, 2011]. Water adsorption energies have been calculated for forsterite, an end member of the olivine solid solution series, by molecular mechanics calculations [De Leeuw et al., 2000], DFT [De Leeuw, 2001], and embedded cluster

[Goumans et al., 2009] approaches. In addition, the temperature programmed desorption (TPD) of water from lunar maria surrogate JSC-1A has been measured previously [*Goering et al.,* 2008; *Hibbitts* et al., 2011]. This work examines JSC-1A and Bancroft albite samples more thoroughly than the other works. We explicitly derive desorption activation energies for the water binding sites of each sample. These derivations are essential for the accurate modeling of the concentration of adsorbed water on these materials and do not currently exist.

2.2 Experimental Details

2.2.1 Temperature Programmed Desorption (TPD) Apparatus

TPD experiments were performed in a stainless steel Ultra-High Vacuum (UHV) chamber (base pressure $<3 \times 10^{-10}$ torr). TPD is a well-known technique for obtaining desorption activation energies from surfaces with adsorbates. The general procedure involves mounting the sample in ultra-high vacuum, cooling to the desired dosing temperature, dosing the adsorbate, and heating the sample at a constant temperature ramp while recording the rate of desorption versus temperature (for more detail on TPD experiments, see for example, *Kolasinski* [2002]). Two authoritative reviews of water TPD from surfaces are given by *Thiel and Madey,* [1987] and *Henderson*, [2002]. Though our TPD approach was briefly described previously [*Hibbitts et al.*, 2011], more details are given here. The UHV chamber is shown schematically in Figure 2.1. The chamber was equipped with a turbo-molecular pump, a quadrapole mass spectrometer (QMS) with a self-contained electron impact ionization source, and a temperature controlled sample holder. This was constructed from an approximately 2 cm × 1 cm × 0.1 cm

oxygen-free copper bar (for high thermal conductivity) that was chemically plated with several microns of nickel and then capped by several microns of gold. The gold provides a hydrophobic surface and chemisorbs very little water, although multilayer water and ice will still readily adsorb at temperatures below 180 K. As shown in the expanded view in Figure 2.1, the holder was mounted horizontally on a steel spring and cooled (minimum temperature <110 K) by mechanical connection with a liquid nitrogen-cooled copper cooling stage. The function of the steel spring is both to provide thermal isolation of the sample holder from the chamber and also to aid in making the

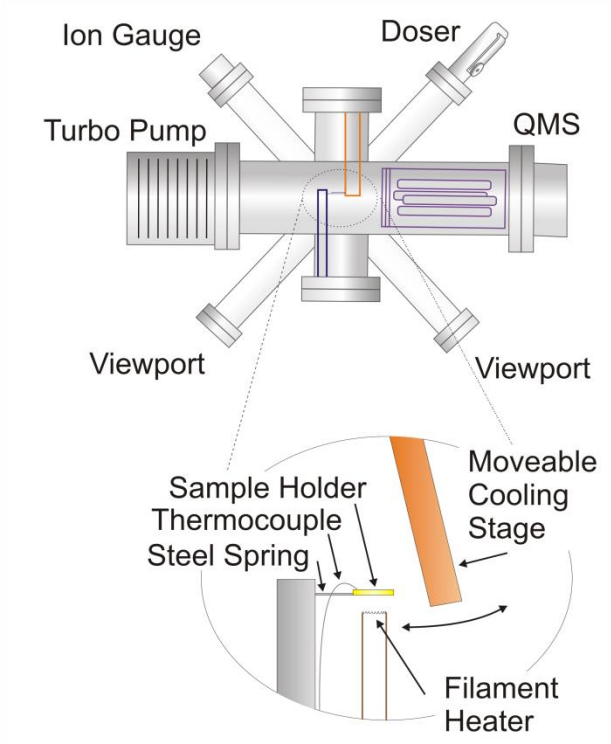

Figure 2.1: Schematic representations of the ultra-high vacuum chamber and the sample holder assembly used for the temperature program desorption experiments.

mechanical connection to the copper cooling stage. Radiative heating was performed by a dual-filament tungsten heater mounted less than 1 cm below the sample holder. Sample temperature was monitored constantly with a type-K thermocouple, which also provided feedback for a computer-controlled temperature ramp, set at 0.5 K/s for these experiments. The measured intrinsic warming rate when the cooling connection was disengaged was less than 0.2 K/s at 110 K and has no effect on the measurement. Desorption of a given mass species was monitored quantitatively with the mass spectrometer. The TPD measurement yields the rate of removal of the adsorbate as a function of substrate temperature and is a well-known technique for obtaining adsorbate desorption activation energies.

To minimize background signal from surfaces other than the sample powders, the cooling stage was mounted on a flexible bellows, allowing it to be in contact for cooling and completely disconnected from the sample holder during the heating phase of the TPD experiments. Dosing was achieved by intentionally leaking pure water vapor (distilled water degassed by multiple freeze-pump-thaw cycles) into the chamber through a leak valve to maintain a controlled chamber pressure for a set amount of time. Exposures of 0.2 Langmuir (L) up to ~ 500 L were employed. A Langmuir is defined as a pressure of 1 x 10^{-6} torr for 1 second and corresponds to approximately 10^{15} collisions with the face of a flat 1 cm^2 surface. Though a Langmuir of exposure is often sufficient to form an adsorbate monolayer on a flat surface, it is insufficient when the sample is a rough and porous film of powder.

2.2.2 Diffuse Reflectance Infrared Fourier Transform Spectroscopy (DRIFTS) Apparatus

DRIFTS experiments were conducted at ambient pressure on a Perkin Elmer Spectrum 1000 with a Perkin Elmer Diffuse Reflectance accessory and nitrogen purge. The spectral range was 2.5 to 25 µm (4,000 to 40,000 cm^{-1} with 4 cm^{-1} resolution). The angle of incidence was 38°, with a collection angle of □ steradians, collecting ~50% of the diffusely reflected energy with less than 5% specular reflectance (as tested by the manufacturer for KBr and KCl). The same aspheric reflector was used for incidence and collection, maximizing reproducibility from sample to sample.

2.2.3 Lunar Regolith Samples

The samples studied were mechanically micronized JSC-1A powder, a well-studied glass/mineral mixture simulating lunar regolith in the maria regions, and Bancroft albite, an analog for plagioclase regolith in the lunar highland regions. Elemental compositions are given in Table 2.1 and further discussion of these materials can be found in *Hibbitts et al.* [2011] and references therein. The powders were derived from coarser samples by wet grinding each material for about 20 minutes in a McCrone® Micronizing mill. Single point nitrogen gas adsorption analyses by the Brunauer, Emmett, and Teller (BET) method [*Brunauer et al.*, 1938] with a Micromeritics Flowsorb III resulted in a surface area of about 8 m^2/g for the micronized JSC-1A, while the micronized albite exhibited a surface area of about 17 m^2/g. These surface areas correspond to nominal particle sizes

Table 2.1 Elemental composition of samples studied, compared to lunar soil*

Sample	SiO_2	TiO_2	Al_2O_3	MgO	CaO	Na_2O	K_2O	Fe_2O_3	Total
JSC-1A	47.71	1.59	13.02	9.01	10.42	2.70	0.82	10.79	96.0(
Albite	63.74	0.01	23.02	0.04	4.47	7.93	1.43	0.18	100.8
Apollo 14	47.3	1.6	17.8	9.6	11.4	0.7	0.6	10.5	99.5

*Table adapted from *Hibbitts et al.* [2011].

of 250 nm for micronized JSC-1A and 130 nm for micronized albite. The purpose of the micronization process was to create defects by breaking up the particles, making the materials more like the highly-gardened lunar regolith. An undesired side effect of this process was that the particles were produced with a higher specific surface area than has been measured for lunar regolith material [e.g. *Robens et al.*, 2007].

About 40-50 mg of the micronized powder was distributed uniformly over all sides of the sample holder by dispersion with methanol and mechanical spreading. This is equivalent to a nominal layer thickness of ~10 μm of powder. Care was taken to cover as much of the holder as possible to reduce any water background from the holder. The use of a thin layer of sample minimizes the chance of repeated re-adsorption of water during a desorption experiment, which might cause peak broadening in the TPD results. Control experiments that varied the powder layer thickness showed an insignificant change in the results when thickness was varied from about 1 to 15 μm. Once the sample had been deposited on the holder, the chamber was sealed, evacuated, and baked at ~400 K for at least 48 hours. During this time, pre-adsorbed water, methanol and atmospheric contaminants were removed from the sample.

2.3 Results and Discussion

2.3.1 Observations from the Pretreatment Process

Figure 2.2 shows the background-subtracted m/z = 18 (H_2O) desorption rate measured by the QMS during the initial heating of micronized albite to 750 K at a ramp rate of 0.5 K/s. These data show at least two overlapping desorption features: a broad feature from the starting temperature of ~ 325 through 425 K and a more prominent

feature centered near 600 K. The 600 K water desorption feature is consistent with reports for recombinative desorption of closely associated "geminal" and “vicinal” hydroxyl groups located at adjacent surface sites [e.g. *D'Souza and Pantano*, 2002]. The sub-425 K feature is at a temperature less than the recombinative desorption temperatures reported for silica and is assigned here as molecularly chemisorbed water. This assignment is also in agreement with calculations for water adsorption on forsterite [*De Leeuw et al.,* 2000; *De Leeuw,* 2001; *Goumans et al.,* 2009], which report maximum molecular water adsorption energies corresponding to desorption around 400 K. No water was introduced to the sample during this experiment and the 600 K feature does

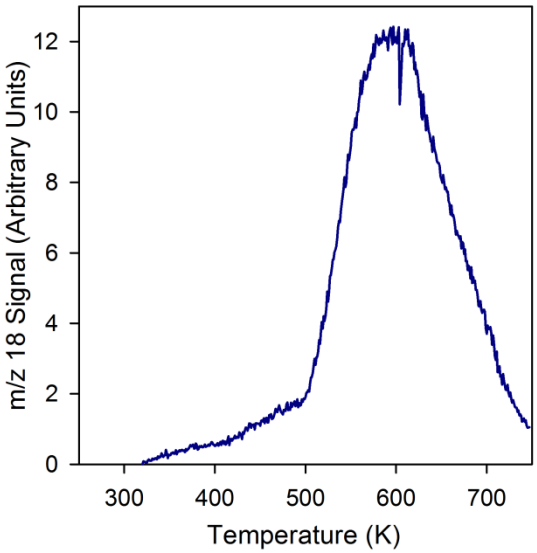

Figure 2.2: Temperature programmed desorption spectrum of water (m/z = 18) collected during the vacuum pretreatment of albite. The pre-425 K feature is consistent with chemisorbed molecular water, while the majority of the signal is consistent with water produced by recombinative desorption of geminal and vicinal hydroxyl groups. Isolated hydroxyls are unlikely to be fully removed at these temperatures.

not return upon subsequent water dosing at low temperatures and pressures. Because dissociative adsorption of water should restore the terminal hydroxyl groups, these results indicate that dissociative adsorption of water does not occur on these previously pre-heated samples under lunar temperatures.

DRIFTS was used to confirm the identity of species removed during initial vacuum heating to 750 K. Unheated, micronized albite was used as a background and the spectrum of micronized albite that had been heated to 750 K under vacuum was then measured under nitrogen purge (taken straight from the UHV chamber to the DRIFTS apparatus). The ratio of the heated powder spectrum to the fresh powder spectrum was taken and produced the solid red line in Figure 2.3. This represents the spectrum of surface species that had been removed by heating to 750 K. Absolute absorbencies for water and hydroxyl are also plotted for reference [*Hibbitts et al.,* 2011]. The ratio spectrum is a poor match to the calculated water-only spectrum (green dash-double-dotted line), but a good match to the experimental spectrum of water and hydroxyl (dashed purple line).

Most adsorbed water desorbs during the initial baking of the chamber during evacuation to ultra-high vacuum, thus, the water release observed during pretreatment is primarily from recombinative desorption of surface hydroxyl groups. The temperature at which they desorbed corresponds to a desorption activation energy range from about 1.2 to 2.1 eV, and may vary ±0.1 eV. Hydroxyl groups were not restored via effusive dosing of water vapor in UHV on laboratory timescales. Furthermore, hydroxyls did not re-form after (i) several hours in ambient air (consistent with *Ichimura* et al. [2011]), (ii)

several hours at ~10 torr of water vapor or (iii) exposure to a few drops of methanol followed by moderate heating in ambient air. Thus, hydroxyls removed during sample pretreatment were either native to the samples as received (cf. data in *Dyar et al.* [2010]) or formed during the micronizing process. The thermal pretreatment produced a sparsely hydroxylated sample surface for the subsequent experiments.

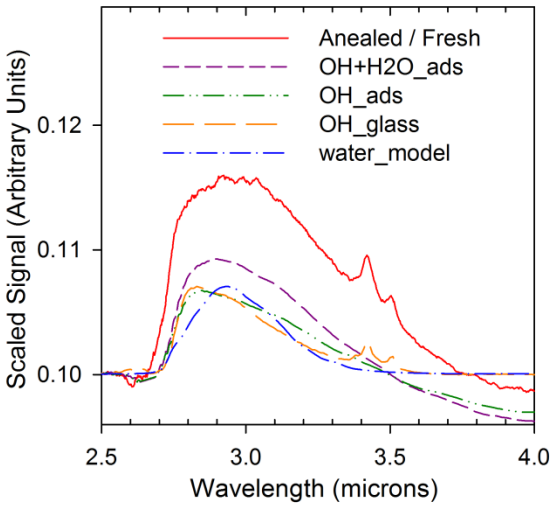

Figure 2.3: Scaled DRIFTS infrared spectra. The solid red line is the ratio of vacuum-annealed albite micronized powder to unheated (fresh) albite micronized powder. This spectrum shows the change in absorbance between the unheated and heated sample. Other spectra are absolute absorbances similar to those in Hibbitts et al. [2011] and are shown for reference. The dashed purple curve is water and hydroxyl on JSC-1A at ambient pressure, the dash-double-dotted green curve is hydroxyl on JSC-1A under vacuum, the long-dashed orange curve is hydroxyl in lunar glass, and the dash-dotted blue line is a modeled absorption spectrum for water. All spectra were collected at room temperature. The ratio spectrum best matches the dashed purple spectrum, which is a combination of water and hydroxyl bands, indicating that both water and hydroxyl are removed by the vacuum treatment to 750 K.

2.3.2 Varied Quantity of Exposure

TPD experiments of pretreated (heated to 750 K), micronized JSC-1A exposed to water at a temperature below 110 K are shown in Figure 2.4. Panels (a) through (c) show an increase in exposure from 0.2 L to 128 L. Figure 2.4a shows that at low exposures (less than 1 L), a broad peak is observed from 170 to ~ 400 K. As is shown in Figure 2.4b, this feature, which we assign as molecular chemisorption, increases in magnitude with continued exposure up to 64 L, and does not stop increasing until an exposure of over 64 L (see Figure 2.4c inset). The simplest explanation of this feature's apparent saturation is that all molecular adsorption sites on the surface have been filled by adsorbed water molecules [*Hibbitts et al.*, 2011]. In addition to the molecular chemisorption feature, a narrow peak with onset at about 140 K begins to appear at 0.5 L. The maximum of this peak shifts to higher temperature as the peak grows, indicating that desorption kinetics are independent of concentration (i.e. zeroth order in equation 2.1 below); the peak is assigned generically as clustered water-ice. The clusters are most likely two- dimensional at low exposures (< 8 L) and grow into three-dimensional clusters when more water molecules are available [*Thiel and Madey*, 1987; *Henderson*, 2002; *Orlando*, 2003].

Data presented in Figure 2.4 confirm and expand upon initial results presented in *Hibbitts* et al., [2011] and are qualitatively similar to those of *Goering et al.* [2008] in that both show ice features at low temperature and a broad desorption signal extending to 400 K. The major difference is that *Goering et al.* observed three distinct peaks emerging from the broad signal, while in the present work no distinct peaks appear

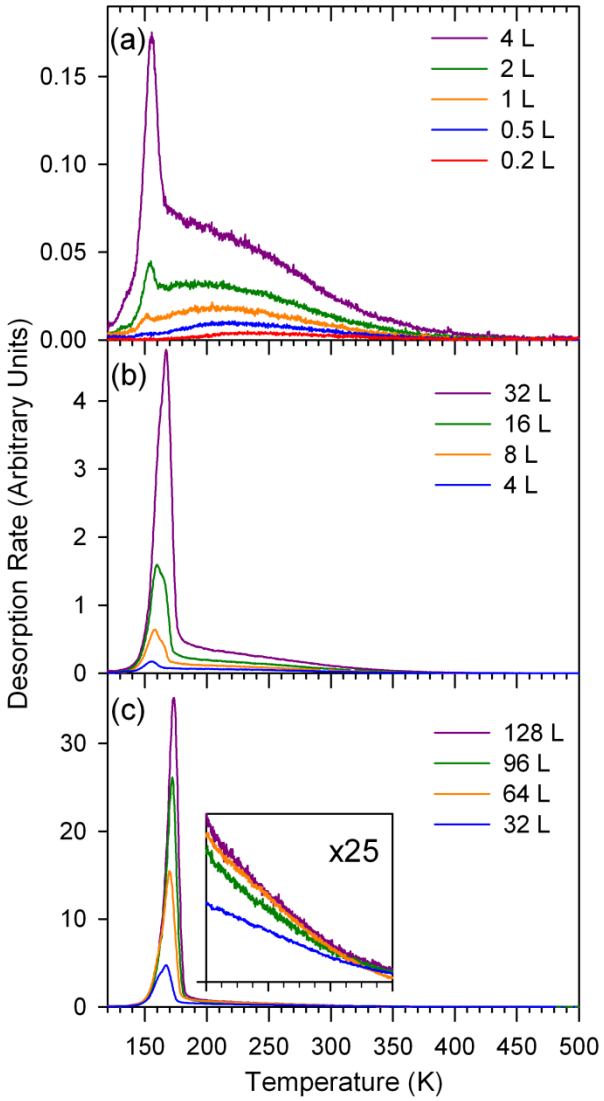

Figure 2.4: Temperature programmed desorption spectra for water dosed on micronized JSC-1A at less than 110K. Doses range from 0.2 to 128 L and are represented by different colored lines. The feature with onset at ~140 K indicates ice formation. Inset shows saturation of the high temperature feature.

beyond those expected for amorphous and crystalline ice. The micronizing process used in the present work produces fine particles with an initially high defect density, so differences between the two datasets may reflect physical differences between the two sample surfaces. The particle identities and densities are most certainly different from those studied by *Goering et al.*; also, as was described in section 2.1, our experimental set-up more effectively minimizes background signals. A direct quantitative comparison of the two datasets is not attempted here.

TPD experiments of pretreated (heated to 750 K), micronized albite exposed to water at a temperature below 110 K are shown in Figure 2.5. Panels (a) through (c) show an increase in exposure from 0.2 L to 128 L. As seen in the JSC-1A experiments, at low exposures (Figure 2.5a) a broad peak is observed beginning at ~170 K and extends to ~400 K. However, increased exposure reveals a defined peak centered around 220 K that was not seen for JSC-1A. We assign this peak primarily to molecularly chemisorbed waters. As shown in Figure 2.5b, higher exposures (> 2 L) result in a deviation from baseline that lasts up to about 425 K. This signal may originate from molecularly chemisorbed water adsorbed at sites more stable (but significantly less abundant) than those responsible for the 220 K chemisorption peak. Unlike the JSC-1A experiments, the chemisorption feature in these experiments shows no sign of saturation even by an exposure of 512 L (see Figure 2.5c inset). This may indicate a significantly larger concentration of water chemisorption sites on the albite polycrystalline particles relative to the partially-glassy JSC-1A. A quantitative comparison of the two sets of results is included in section 2.3.5.

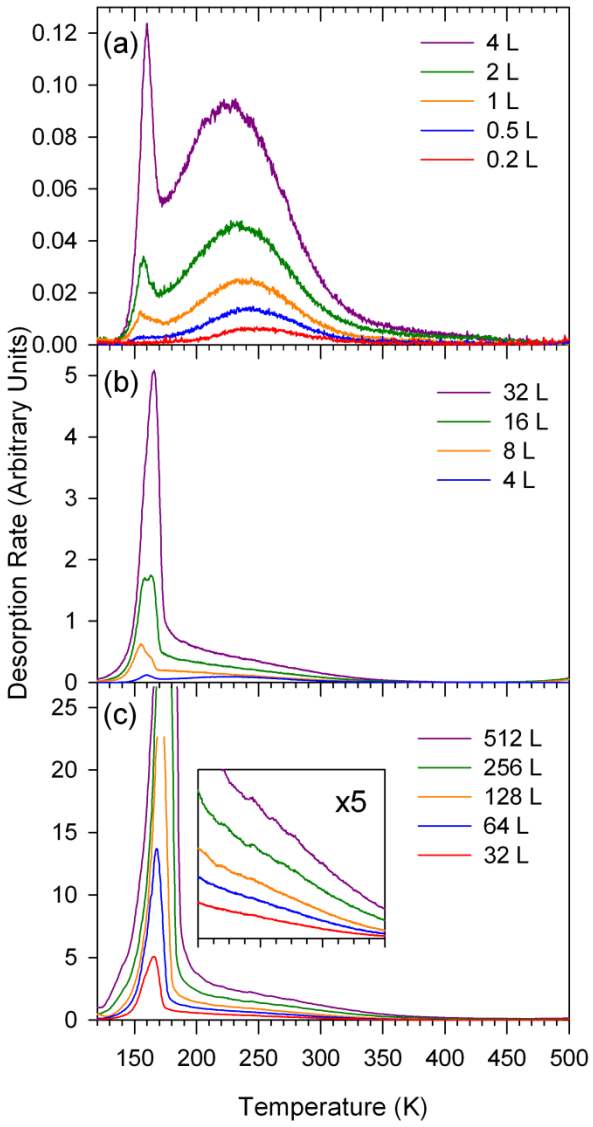

Figure 2.5: Temperature programmed desorption spectra for water dosed on micronized albite at less than 110 K. Doses range from 0.2 to 512 L and are represented by different colored lines. The feature with onset at ~140 K indicates ice formation. Inset shows that the high temperature feature is not saturated.

2.3.3 Varied Temperature of Exposure

JSC-1A is a heterogeneous mixture of different phases, so it is likely that a distribution of pores and defect sites exists, each surrounded by a slightly different surface landscape and having its own desorption activation energy for chemisorbed water. Desorption from a distribution of sites will sum to a broad peak, similar to those observed in Figures 4 and 5. However, if ice formed within pores in the powder film, the water must then undergo a multi-step random walk before desorbing. Such a process could cause ice desorption to appear at a higher temperature during the TPD, although with a ramp rate of 0.5 K/s, a delay of just 20 K would require 40 s of retention, which is unlikely because of the thinness of the powder layers, however, we investigated this possibility nonetheless. To differentiate between a distribution of chemisorption sites versus ice desorption broadened by the random walk to vacuum, water was dosed at elevated temperatures (140-440 K) where little or no ice should form. The sample was then held at the dosing temperature for about 5 minutes while the residual water was pumped out of the chamber before finally cooling the sample to 110 K and starting the TPD as usual. If the broad peak was from ice desorption followed by a random walk as the vapor traveled out of the powder film, then exposure to water at temperatures greater than ~ 150 K should reduce water adsorption, and the TPD would be closer to the baseline signal for the entire trial. Clearly, if any water desorption is measured above the dosing temperature, it would indicate the existence of chemisorption sites with sufficient binding strength to retain water at moderately elevated temperature.

TPD experiments of JSC-1A with 2 L water exposure at temperatures ranging from 110 to 340 K are reported in Figure 2.6. With a 140 K dosing temperature, only a small portion of the ice remains while the broad peak is indistinguishable from the 110 K data by 200 K. Dosing at increasingly warmer temperatures removes the portion of the peak below the dosing temperature but traces the 110 K data very well above the dosing temperature. This supports the interpretation that the broad peak is from a distribution of chemisorption sites that are accessed either during dosing or desorption. Even at a dosing temperature of 340 K, the water signal at temperatures above 340 K remains. In fact, a water desorption peak was observed with a dosing temperature of 400 K, but not with a dose at 420 K; those data are not shown.

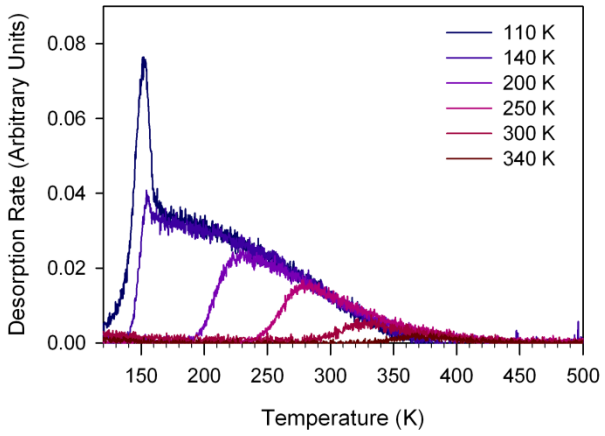

Figure 2.6: Temperature programmed desorption spectra from 120 K to 500 K for 2 L water exposure at elevated temperatures on micronized JSC-1A. Dosing temperatures ranged from 110 K to 340 K and are indicated by different colored lines. The broad desorption from 170 to 400 K is primarily from chemisorbed waters.

TPD experiments on albite with 2 L water exposure at temperatures ranging from 110 to 340 K are shown in Figure 2.7. The 200 K data do not trace the 110 K data as well as they did on the JSC-1A, which may indicate some broadening due to water trapping in pores and/or spaces between grains. Some of the water that normally would have desorbed from chemisorption sites between 150 and 200 K may be retained in pores and show up in the TPD after 200 K. Regardless of whether a small amount of broadening is occurring, the data in Figure 7 support assignment of the broad peak primarily to molecularly chemisorbed water. Similar experiments performed at 64 L exposure showed analogous results.

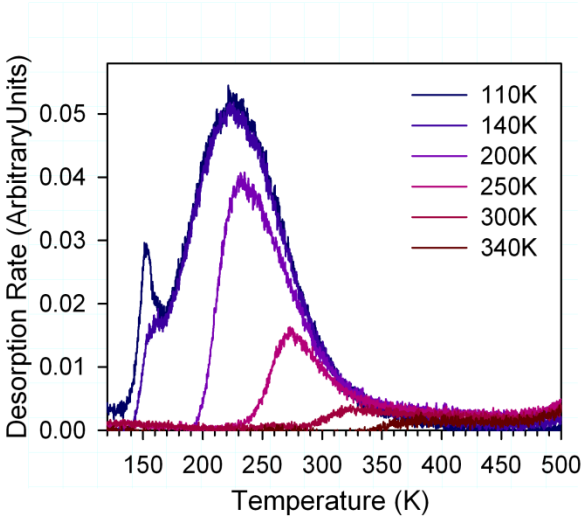

Figure 2.7: TPD spectra from 120 K to 500 K for 2 L water exposure at elevated temperatures on micronized albite. Dosing temperatures ranged from 110 K to 340 K and are indicated by different colored lines. The broad desorption from 170 to 400 K is primarily from chemisorbed waters, with the possibility of a small contribution (seen as peak broadening) resulting from multiple chemisorption and desorption events in non-surface sites due to the high porosity of the sample.

2.3.4 Isothermal Desorption Measurements

Isothermal TPD was also performed to test the existence of water adsorption sites corresponding to the broad chemisorption feature from 170 to 400 K. Isothermal TPD consists of dosing at low temperature (in this case, ~115 K), followed by cycles of rapid heating alternating with measurement of water desorption while holding the sample at constant temperature. The utility of the isothermal TPD process in this case is that allowing the desorption rate to decay at a given temperature makes certain that any desorption at the next temperature step is from more strongly bound adsorption sites than the previous step. Isothermal TPD from both samples with 4 L exposures confirmed that the measured desorption signal is dominated by chemisorbed sites and not readsorption or diffusion during the TPD. A representative section of the isothermal TPD of albite is shown in Figure 2.8.

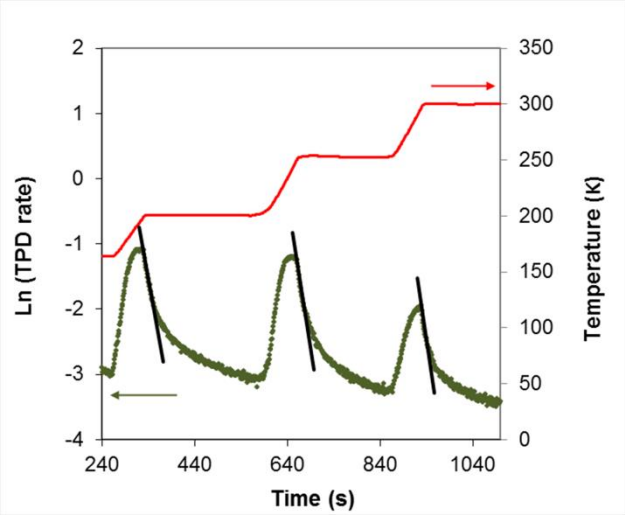

Figure 2.8: Representative section of the isothermal desorption spectrum collected following a 4 L water exposure at 120 K on micronized albite powder. The sample temperature is represented by the red line, the natural log of the water desorption rate is represented by the green diamonds, and the black lines represent the linear fit to the isothermal falling edges of the peaks. The left axis describes the isothermal desorption rate whereas the right axis describes the temperature ramp.

The desorption kinetics of adsorbed molecules from a surface are described by the Polanyi-Wigner equation:

$$\frac{dN}{dt} = -kN^n, \tag{2.1}$$

where *N* is concentration (or coverage), *t* is time, *n* is the order of desorption, and *dN/dt* corresponds to the signal measured by the QMS in the TPD experiment. The rate constant, *k*, comes from the Arrhenius equation:

$$k = Ae^{-E_d / k_B T} \tag{2.2}$$

and is a function of temperature, T (in Kelvin), and the desorption activation energy, E_d (in eV). *A* is a pre-exponential factor, here assumed to be a constant 10^{13} Hz (see *Kolasinski* [2002] or *de Jong and Niemantsverdriet* [1990] for more information about pre-exponential factor choice), and k_B is the Boltzmann constant. For first order desorption (i.e. *n*=1, as is the case for desorption of adsorbed molecular water), plotting the natural log of the measured desorption rate versus time and fitting the isothermal falling edge of each peak with a straight line yields the rate constant, *k*, from the following rearrangement of equation 2.1:

$$\ln(N) = -kt + \ln(N_0). \tag{2.3}$$

Because of the complex nature of the sample surface, isothermal desorption is a convolution of multiple desorption centers, each desorbing with its own rate. Fitting only the leading edge of each desorption peak captures those centers desorbing most rapidly, allowing isolation of the sites most closely associated with the isothermal

temperature. Using the average slope of these lines in equation 2.2 and solving for desorption activation energy yields the following equation for both samples:

$$E_d = 0.003T, \tag{2.4}$$

where E_d is in eV per molecule and T is in units of Kelvin. For example, this yields values of 0.5 eV for desorption at 170 K and 1.2 eV at 400 K.

2.3.5 Obtaining the Energy Distribution of the Adsorption Sites

Analysis of several isothermal TPD traces has been carried out, indicating a distribution of activation energies as expected. However, quantifying the relative number of each desorption site from overlapping TPD peaks requires a numerical analysis approach. The numerical analysis was performed following *Barrie* [2008], using a custom data-fitting program written in National Instruments Labview 8.6. The output from the program yields a distribution function that expresses the differential concentration of adsorption sites corresponding to a bin centered at a given energy. Because thermal desorption while heating is an ill-posed problem, the distribution function was obtained iteratively. First, an initial approximation was obtained by the condensation approximation [*Barrie*, 2008]. The resulting distribution function, $N_0(E)$, was used to generate a TPD spectrum by means of the Polanyi-Wigner equation (equation 2.1 above). The simulated TPD was compared to the experimental TPD and the distribution function was systematically varied until the value of *z*, the least squares error between the modeled activation energy and measured energy, coupled with a smoothing function

$$z = rss + \lambda p \tag{2.5}$$

was minimized. Here *rss* stands for the residual sum of squares:

$$rss = \sum_{j=1}^{n} [r_d(T_j) - r_{pred}(T_j)]^2, \tag{2.6}$$

where r_d and r_{pred} are the measured and modeled desorption rates, respectively, for a given temperature point, T_j, and λ is a fitting parameter. A penalty function, p, is defined as:

$$p = \int_0^{\infty} \left[\frac{d^2 N_0(E)}{dE^2} \right]^2 dE, \tag{2.7}$$

where N_0 is the number density from the distribution function at a given desorption activation energy, E.

The purpose of the penalty function is to smooth out erratic variations that often occur when minimizing only the *rss*. The parameter, λ, finds the optimal level of smoothing where the distribution function results in a good match to the experimental TPD while not being too erratic. *Barrie* [2008] includes a discussion of the different means of choosing λ. In this work, λ was chosen by a combination of the "L-curve" and "by eye" methods.

An alternative method for calculating the apparent distribution of adsorbate desorption energies has been suggested by *Dohnálek et al.* [2001]. This method accounts for the fact that many adsorbates can undergo lateral interactions with other nearby adsorbate molecules while building up the initial adsorbate monolayer. However, broad desorption peaks in TPD spectra of systems involving lateral interactions tend to progress from high temperature to low temperature with increasing coverage (ex. [*Dohnálek et al.* 2001]) and the spectra here do not. Figures 2.4 and 2.5

show TPD spectra of self-similar curves, comparable to the hydrogen TPD results of *Vidali and Li* [2010]. Hydrogen is incapable of lateral interactions and the remarkable similarity between the two sets of results is consistent with the plausibility of minimal lateral interactions occurring in the present system. While lateral interactions are the norm for adsorbed water at high coverage, the effective coverages in these experiments are less than half a monolayer, a regime where isolated adsorbed water molecules are statistically plausible. The numerical analysis method described above is the best currently-known method for obtaining the distribution of desorption activation energies for non-interacting adsorbed species. Though this method is very useful for obtaining the distribution function, it lacks any direct treatment of the complex morphology of the sample.

The morphology and porosity within the powders have not been examined, leaving the importance of water readsorption during the TPD experiment as an unknown in interpreting the experimental results. Two extreme cases can be considered to set bounds on the importance of readsorption: (i) when adsorbate residence times are negligibly short on the experimental timescale and (ii) when adsorbate residence times are sufficiently long that only the external surface of the powder bed is probed during the TPD experiment. In case (i), the entire powder bed will be probed by the water during the course of an experiment. Thus, the chemisorbed water will desorb from sites spread over the entire 40 – 50 mg of deposited sample. Case (ii) is essentially equivalent to exposing only the external ~5% of sample to water. The concentration of water within the powder would approximate a step function with ~1000 ppm in the first layer

and ~0 ppm deeper into the powder. The external concentration is highly dependent on the external surface area, which in turn requires detailed information on the powder morphology. The similarity, as was discussed above, between the present TPD spectra and those reported by *Vidali and Li* [2010] for hydrogen is consistent with case (i), but not case (ii), which will not have isolated adsorbed water molecules. Thus, case (i) will be assumed for the remainder of this chapter.

2.3.6 Obtaining the Adsorbed Water Concentrations

The distribution function obtained from the above procedure can be seen in Figure 2.9a. The conversion from arbitrary units to units of concentration requires knowledge of the total water adsorbed at 64 L and >512 L for the micronized JSC-1A and albite, respectively. As mentioned in Section 2.1, one Langmuir of exposure statistically corresponds to approximately 10^{15} molecule collisions with the face of a flat 1 cm^2 surface -- sufficient molecules to form an idealized monolayer. However, 40 mg of micronized JSC-1A particles have a total surface area of 3,200 cm^2. When spread evenly over 7 cm^2 of sample holder surface, this effectively enhances the surface area by a factor of ~ 460 compared to a flat surface; i.e. the exposure required to saturate an ideal monolayer in this geometry is estimated to be ~ 460 L (assuming unity sticking and no ice formation). Assuming the effective surface area of an adsorbed water molecule to be ~10 $Å^2$, the concentration of water in an idealized monolayer is ~ 2400 ppm (by mass) for micronized JSC-1A and ~ 5100 ppm (by mass) for micronized albite. Thus, a 64 L exposure will result in an adsorbed water concentration of ~ 336 ppm (by mass) on the micronized JSC-1A powder. Similar analysis using a 512 L water exposure on 50 mg of

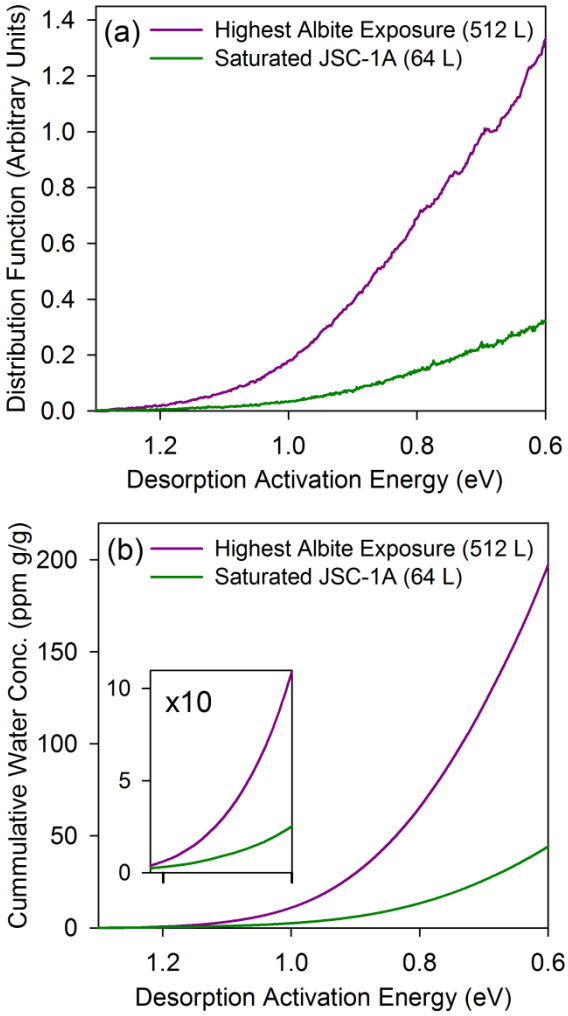

Figure 2.9: Distribution function of desorption activation energies expressed both as (a) differential concentration and (b) cumulative concentration from high to low desorption activation energy. The inset in panel (b) is a ten times magnification of the curve from 1.2 to 1.0 eV. Assumptions used in obtaining the distribution function included: (1) readsorption during the TPD experiment was negligible, and (2) the entire powder deposited had been exposed and saturated with water. With these assumptions, a small amount of water desorbs with activation energy approaching 1.2 eV. These plots show that there a very few sites with high binding energies and that >90% have energies less than ~0.9 eV.

micronized albite results in a lower bound for the water concentration of ~ 2200 ppm (by mass). These values correspond to the water concentration represented by the area under the distribution function, which in turn enables the conversion from arbitrary units to units of concentration.

Figure 2.9b contains the cumulative distribution function in units of concentration. Summing just the energies that correspond to chemisorption (i.e., those above the ice sublimation energy) yields ~62 ppm of chemisorbed water on micronized JSC-1A and ~ 220 ppm on micronized albite. These results show that the polycrystalline albite particles can chemisorb about four times more water by mass than the mineral and glass JSC-1A 'soil' particle mixture at any given temperature. However, normalizing to equal surface area brings the difference in adsorptive capacity between the two samples down to a factor of two.

2.4 Application of Experimental Results to the Moon

The samples used in these experiments were micronized to better simulate the high surface defect concentration of the lunar regolith. However, this process increased the sample surface areas by about an order of magnitude relative to the surface area of lunar regolith. Assuming a surface area of 1 m^2/g for the lunar regolith (ex: [*Hibbitts et al.*, 2011] and references therein), adjustment of the concentrations obtained above yields saturations of ~ 5 ppm and 12 ppm for chemisorbed water in the lowland mare and highland anorthositic terrains, respectively. Note that while JSC-1A is derived from a volcanic ash of basaltic composition, chosen and scaled to reproduce the chemistry, mineralogy, and particle size distribution of low-Ti mare soil, it is not identical. In

particular, this simulant is known to have roughly 2.0 wt. % more Na_2O than a typical lunar soil, and volatile contents of 0.71 wt% as measured by loss on ignition, likely a combination of H, S, Cl, and C (*McKay et al.,* 1994).

The Visual and Infrared Mapping Spectrometer (VIMS) aboard NASA's Cassini spacecraft, the Deep Impact High-Resolution Instrument–infrared spectrometer, and NASA's Moon Mineralogy Mapper (M^3) instrument aboard India's Chandrayaan-1 all observed the lunar surface and reported a 3-µm absorption, which was attributed to water and/or hydroxyl. VIMS and Deep Impact spectra contained features reported as varying quantities of water at all latitudes [*Clark*, 2009; *Sunshine et al.*, 2009] while M^3 spectra contained 3-µm absorption primarily at high latitudes [*Pieters et al.*, 2009] greater than about 60º [*McCord et al.*, 2011]. Estimated water concentrations on the order of 10-1000 ppm were reported by Clark, a maximum of 770 ppm was reported by *Pieters et al.*, and up to 5000 ppm at the North pole was reported by *Sunshine et al*. These values are up to three orders of magnitude higher than the concentrations of chemisorbed water measured in the present experiments. Furthermore, even on laboratory timescales (heating cycles required less than half an hour), the vast majority of adsorbed water desorbs at temperatures well below the typical temperatures of the lunar dayside (up to 400 K).

The quantity of water that would persist (i.e. not desorb) on a surface grain through lunar temperature conditions on lunar heating timescales (~14 Earth days) was estimated based on the experimental results in this paper. The change in water concentration with time can be represented by the Polanyi-Wigner equation (equation

2.1 above). Assuming first order kinetics (molecular chemisorption; n = 1) yields the following solution to equation 2.1:

$$N = N_0 e^{-k\Delta t}, \tag{2.8}$$

where N_0 is initial concentration and Δt is elapsed time. Starting with a surface that is saturated with water and making use of lunar temperature data [*Vasavada et al.*, 1999] interpolated as a function of latitude and time of day, desorption of chemisorbed water throughout a summer lunar day was calculated for several high latitudes. The calculation neglects destruction of water while adsorbed on the surface (such as by high energy radiation), photodesorption, and all transport of water both vertically (in and out of the bulk regolith, cf. *Grieves et al.*, [2010]; *Hibbitts et al.*, [2011]) and laterally over the surface of the Moon (cf. *Crider and Vondrak*, [2000]; *Hurley*, [2010]). Essentially, the calculation method assumes thermal desorption is the only loss term and that any water molecule that desorbs is lost forever from the system and has a negligible chance to readsorb. This is further simplified because no source terms are assumed beyond the initial saturation coverage at local midnight.

The concentrations of persisting water on micronized JSC-1A (normalized to 1 m^2/g) through the lunar day are estimated for several lunar latitudes and are shown in Figure 2.10. Each desorption activation energy bin from the distribution function shown in Figure 2.9a was propagated individually and the sum of all bins at a given time was plotted versus elapsed time. Given an initial nighttime accumulation of adsorbed water equivalent to saturation, the water concentrations fall rapidly just after dawn and continue to fall as the temperature rises throughout the lunar morning. Contrary to

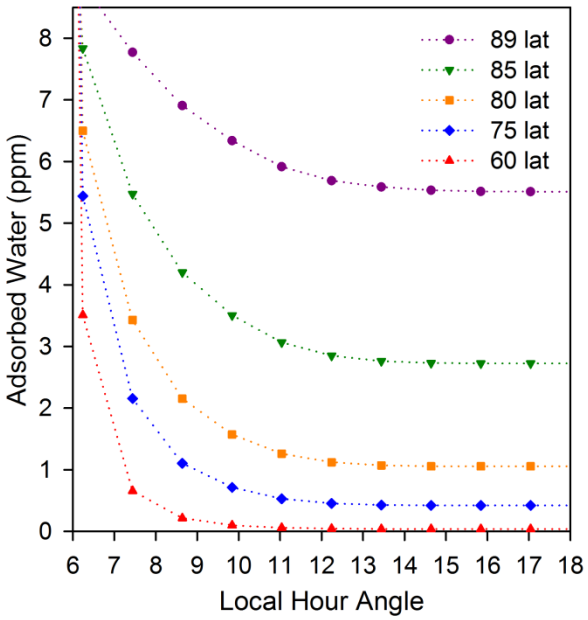

Figure 2.10: Calculation estimating the persistence of adsorbed water on JSC-1A as a function of lunar time of day. The saturated distribution function from Figure 2.9, normalized to a lunar specific surface area of 1 m^2/g, was the initial condition. This calculation neglects photodestruction of water while adsorbed on the surface, photodesorption and other space weathering effects, other inputs of water, and all transport (diffusion) of water both vertically and laterally over the surface of the Moon. While chemisorption will allow small amounts of water to persist for geologically short timescales at locations too warm for any water-ice on the sunlit lunar surface, these concentrations are likely too low to be seen as a 3-µm absorption by remote sensing. However, water may show up in remote sensing due to vertical diffusion and/or a day-time replenishing source.

models considering only ice sublimation (i.e. neglecting water chemisorption), small amounts of water are predicted to persist through the lunar day at temperatures above 150 K. Persisting concentrations stabilize after mid-day and essentially no further water is lost by thermal desorption as the temperature drops throughout the afternoon. Given a sufficient source of migrating water to saturate the regolith each night, the

concentrations shown in Figure 2.10 for a given time of day qualitatively predict the minimum water available to be seen by infrared remote sensing each day on the Moon. The distribution function of desorption activation energies measured predicts no water at latitudes below ~ 60°, generally consistent with the M^3 instrument results [*McCord et al.,* 2011]. However, the water concentrations estimated here are likely too low to be seen as a 3-μm band in infrared spectral measurements. Without readsorption or replenishment, water loss continues approximately exponentially each day, and all surface grains on the illuminated Moon will drop below 1 ppm of adsorbed water within a few hundred lunations. Note that this approach is solely based on thermal desorption. Vertical diffusion and/or a day-time replenishing source could lead to sub-surface water that might show up in remote sensing.

When comparing results from lunar surrogates to actual lunar observations, it is important to remember that while the mineralogy may be similar in both cases, the chemical nature of the grain surface itself can vary in significant ways between a terrestrial surrogate and a genuine lunar soil. For example, *Wallace et al.* [2009] found the surface reactivity of lunar soil to be about four times greater than that of JSC-1A. However, these experiments were conducted in air and do not represent conditions found on the Moon. These values approximate the water that could be available for detection by remote sensing and demonstrate the utility of including the distribution of molecular chemisorption sites in future, more sophisticated models of surficial lunar water abundances.

If the lunar regolith expresses the same distribution of water desorption activation energies as the terrestrial surrogates, but in greater concentrations, then the expected water concentrations reported in Figure 2.10 would tend to increase in magnitude, but the qualitative trends with temperature and latitude would remain about the same. However, if the lunar regolith expresses a distribution of water desorption activation energies that extends to higher energies than the micronized surrogates, not only would the expected water concentrations on the lunar dayside increase, but they would also shift to lower latitudes and higher temperatures. Thus, tracking desorption activation energy is important for modeling lunar water dynamics. For example, water adsorbed at a 1.2 eV site has a theoretical residence time of thousands of seconds at 350 K, while the residence time for water adsorbed at a 0.9 eV site is less than a second at the very same temperature. Because these are lunar regolith surrogates, it is important to extend the methods developed in this work to the lunar samples returned by the Apollo and Luna missions; this work is currently in progress.

2.5 Conclusions

Interactions of molecular water with lunar regolith surrogates (micronized JSC-1A and albite) were examined using TPD and DRIFTS. TPD revealed water desorption during initial heating to 750 K under ultra-high vacuum and DRIFTS indicated possible water formation via recombinative desorption of native hydroxyls above 425 K. Dissociative chemisorption of water (i.e. formation of surface hydroxyl sites) was not observed on laboratory time scales after controlled dosing of samples (initially heated above 750 K) with 0.2 – 500 L exposures of water. However, both pre-heated samples were found to

have a distribution of molecular water chemisorption sites, with albite having at least twice as many as the JSC-1A samples by mass. Fitting the TPD data generated a distribution function of desorption activation energies ranging from ~0.45 eV (water-ice clusters) up to 1.2 eV. The desorption activation energies and water concentrations calculated from the TPD data were used to estimate water concentrations expected on the Moon at varying latitudes, assuming water saturation occurs each night. The estimated water concentrations are of only ~ 5 and 12 ppm for chemisorbed water in the lowland mare and highland anorthositic terrains, respectively. These values are well below those reported from spacecraft and ground-based observations.

CHAPTER 3

Measurement of Water Desorption Activation Energies from Apollo Lunar Samples

3.1 Introduction

The presence or absence of hydration on Earth's moon has been a topic of much discussion dating back to at least the beginning of the space race. *Watson et al.* [1961] predicted accumulation of water-ice in the cold permanently shadowed regions (PSRs) at the lunar poles. Lunar samples brought to Earth by the Apollo missions were analyzed for hydration [*Gibson and Johnson*, 1971] and initially found to have hydrogen from the solar wind and water from terrestrial contamination (e.g. *Epstein and Taylor* [1974] and refs. therein). Advanced techniques have more recently found traces of ancient lunar hydration deep within grains of lunar samples [*Saal et al.*, 2008; *Greenwood et al.*, 2011a; *Greenwood et al.*, 2011b; *Liu et al.*, 2012; *Hui et al.*, 2013]. Discussion of lunar hydration recently returned to the public eye when observations by several spacecraft-based experiments were interpreted in terms of hydrated species on the Moon. Three of these observations were of absorption bands near 3 μm in reflected sunlight that are consistent with mineral-bound hydroxyl and possibly water within the first few micrometers of lunar surface materials [*Clark*, 2009; *Pieters et al.*, 2009; *Sunshine et al.*, 2009]. A second set of spacecraft-based observations were of water-ice particles, water molecules, hydroxyl, hydrogen molecules, and atomic hydrogen in the ejecta plume

from the LCROSS impact experiment in a lunar PSR [*Colaprete et al.*, 2010; *Gladstone et al.*, 2010].

Hydration can appear on the Moon in three broad varieties: 1) ancient hydrogen incorporated into minerals as hydroxyl or structural water, 2) cold-trapped water and hydrogen of ancient or modern origin in PSRs and possibly below the thermal skin depth at high latitudes (eg. *Vasavada et al.* [1999]), and 3) surfacial hydrogen from solar wind implantation seen as H, SiH, SiOH, H_2, and possibly H_2O. Each of these reservoirs of hydration can have limited exchange with the others via diffusion and migration promoted by thermal cycling, radiation-induced desorption, and impact events. Understanding the abundance and distribution of lunar hydration is important for scientific understanding of the history and present workings of the solar system.

Lunar hydration, and the forms that it takes: H_2O, OH, H_2, or H, are of great interest to groups seeking to establish permanent lunar bases and interplanetary refueling depots. All forms of hydration are useful for in situ resource utilization (ISRU), because utilization of this hydrogen can reduce the mass of hydrogen that must be brought from the Earth. Oxygen is in plentiful supply on the Moon, but it is incorporated into the silicate minerals and requires energy and hydrogen to remove. Hydroxyl and especially water are most sought after for ISRU because they have the bonus of potentially reducing the amount of energy required to remove oxygen from the lunar soil.

In this work we focus on surfacial water, as has been potentially observed by remote sensing of the 2.95 µm band. During reflection, the infrared radiation penetrates several µms into the material, sampling not just water adsorbed to the grain surface itself, but

also any water trapped inside the mineral or its weathered rim. This work is only considering the adsorbed water, which is capable of migration. General water adsorption behavior on damaged mineral surfaces, such as those found on fine, weathered lunar soil grains, has been reviewed previously [*Hibbitts et al.*, 2011]. Water adsorption and desorption from lunar simulant JSC-1A [*Goering et al.*, 2008] and mechanically-micronized JSC-1A and albite [*Hibbitts et al.*, 2011; *Poston et al.*, 2013] (see Chapter 2) have been previously measured. In this work we present results of water adsorption and desorption from Apollo lunar samples.

3.2 Experimental

3.2.1 Sample Description

A diverse suite of lunar soils was requested from the 'reference suite' of soils sampled by the Apollo and Luna missions [*Heiken et al.*, 1991], which had been divided into five categories by the present authors. Five samples were allocated, one from each category: high-Ti mare soil 10084; low-Ti mare soil 12001; KREEPy soil 14163; mixed mare/highland soil 15221; and highland soil 72501. The samples analyzed here are the sub-90 μm fractions of Apollo lunar samples 72501 and 12001. These two samples were analyzed first with intention to compare the water desorption behavior between highlands and mare materials. 23 mg of sample 72501, a mature anorthositic soil, and 28 mg of sample 12001, a sub-mature low-titanium basaltic soil, were used for the analysis. The fines fraction was used here to maximize surface area, which maximized absolute signal from the sample. Sample 72501 is relevant to the water adsorption behavior of the lunar highlands. Sample 12001 was requested to be relevant to the water adsorption behavior of the mare. However, after sample 12001 was analyzed, the authors learned that, according

to the Lunar Sample Compendium [*Meyer C.* (2011) available online at http://curator.jsc.nasa.gov/Lunar/lsc/index.cfm, accessed on 04/03/2014], the vacuum vessel containing sample 12001 was found to have ~ 5 x10^{-2} torr of gas pressure when it arrived at the Lunar Research Laboratory. At this pressure the entire sample would have been rapidly contaminated and the sample surface may have had the opportunity to passivate. This will be discussed in the context of the experimental results in section 3.2. Further details regarding the samples may be found in the Lunar Source Book, the Lunar Sample Compendium, and references therein.

3.2.2 Experimental Procedures

The experimental procedures and apparatus have been described previously [*Hibbitts et al.*, 2011; *Poston et al.*, 2013] (see also section 2.2.1). The standard procedure for temperature programmed desorption (TPD) experiments is to mount the sample in ultra-high vacuum (UHV), cool the sample to the desired dosing temperature, expose the sample to the desired adsorbate, and then heat the sample at a constant rate of temperature in time while monitoring the desorption with a quadrapole mass spectrometer. (Note: One Langmuir (L) of exposure represents the statistical expectation of 10^{15} molecules of water arriving at a 1 cm^2 area. If the sticking probability is unity and no clustering occurs, this would correspond to a water coverage of 1 monolayer (ML). In the case of a powdered or porous sample, the 10^{15} molecules per Langmuir are spread over more than 1 cm^2 of surface area and correspond to much less than a monolayer. This is the case here.) Briefly, the apparatus consisted of a UHV chamber (base pressure < 3 x 10^{-10} torr) equipped with: a sample holder and detachable cooling stage capable of cooling the sample to 100 K and heating to 800 K as measured

on a type-k thermocouple, a leak valve for exposing the sample to water, an ion gauge to measure chamber pressure, and a quadrapole mass spectrometer for quantifying the water desorption during the TPD.

Previously for the proof-of-concept work [*Hibbitts et al.*, 2011; *Poston et al.*, 2013] (see also section 2.2.2) the surrogate samples were rough spheres of average equivalent spherical diameter 100-200 nm. A result of the small size was that the particles adhered to the sample holder so well that they were placed on both the top and bottom sides of the horizontally-positioned holder. Covering such a large percentage of the holder with sample increased total signal from the sample substantially and all but eliminated background signals during the TPD. The lunar samples, on the other hand, were highly irregular and of much larger grain size, on the order of 10's of micrometers. Such large particles are unlikely to adhere well to the holder, so adjustments were made to the design.

The modified sample holder consisted of a copper bar of about 1 mm thickness wrapped in gold foil to cover the copper bar and form a shallow cup. The purpose of the gold foil was both to form the side walls of the cup and to have as hydrophobic of a holder as possible to reduce water chemisorption background signals. Water-ice can still form on the gold foil at low temperatures, but chemisorption on gold foil is minimal. However, since the sample powders did not adhere well to the gold foil, the sample could only be made to cover about 1-2 cm^2 of the about 10 cm^2 total geometric surface area of the sample holder. This effectively increased the magnitude of the blank by a factor of ~10, and it was seen that the blank signal was about half of the total signal

during a TPD (ex: Figure 3.1). Therefore, blank TPD's were conducted under the same conditions as each sample exposure and subtracted from the sample trials to isolate signal only from the sample. There was also a tail associated with the heater seen at the high temperature end of each TPD, which varied randomly throughout each day. It was found that the tail could be fit with an exponential curve and this curve subtracted to reveal the point at which the TPD returned to baseline.

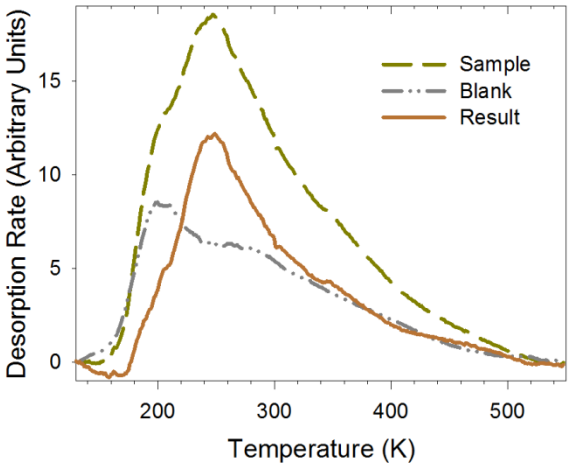

Figure 3.1: Example of the blank subtraction process showing the relative magnitude of the total signal (gold) to the signal from an identical trial performed on the blank sample holder (silver) and the result of subtracting the blank from the total signal (copper). The result is the signal that originates from the sample itself.

3.3 Results and Discussion

3.3.1 Detection of Chemisorbed Water by TPD

TPD experiments of lunar sample 72501 exposed to water at 165 K are shown in Figure 3.2. When water exposure was performed at 110 K, the large quantity of ice desorption from the sample holder made the chemisorption signals very difficult to

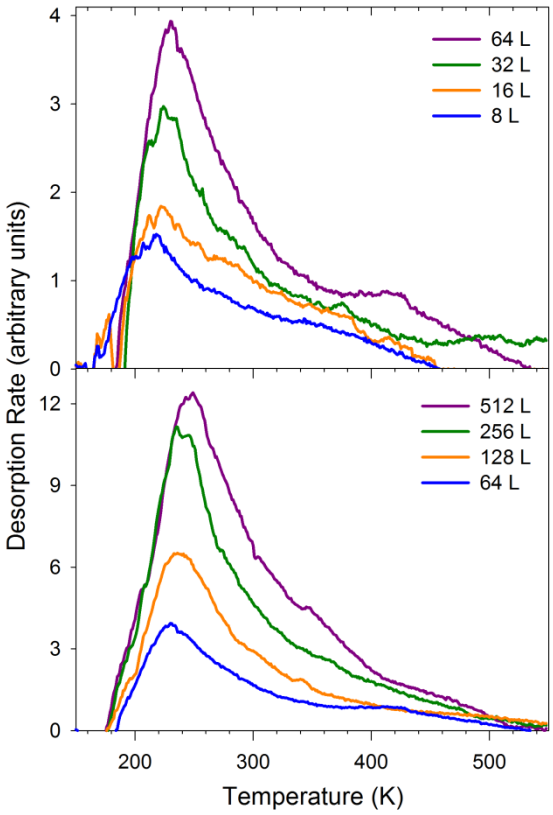

Figure 3.2: TPD spectra for water dosed on the sub-90 µm fraction of Apollo lunar soil sample 72501 at 165 K. Data have been corrected for both heater and blank contributions.

isolate. 165 K is just warm enough to prevent ice formation in UHV, so dosing at this temperature reveals the contributions from chemisorbed water.

Exposures on sample 72501 varied from less than 8 L up to 512 L. Upon heating, adsorbed water begins to desorb around the dosing temperature of 165 K, peaks around 250 K and tails gradually back to baseline. Figure 3.2a shows the highest water desorption at 500 ± 50 K, however, the larger exposures shown in Figure 3.2b indicate that desorption continues to above 500 K on the timescale of the TPD experiment (minutes). The high temperature sites are of greatest interest for the retention of water

on the Moon, because they retain water longer than low temperature sites. Thus additional trials with water exposure at 250 K were conducted to verify their presence (data not shown). Dosing at a higher temperature (250 K rather than 165 K) eliminates desorption from lower energy sites, allowing verification of the sites requiring higher energy to desorb. The trials with water exposure at 250 K showed return to baseline between 500 and 550 K, consistent with the presence of higher energy binding sites. It was shown previously for lunar soil surrogates [*Hibbitts et al.*, 2011; *Poston et al.*, 2013] that broad peaks of this nature (one peak stretching from 165 to 550 K) are the sum of overlapping desorption peaks from a variety of adsorption sites, each with their own unique desorption activation energy. The analysis of the energetics will be performed in section 3.3.2 below.

It can be seen in Figure 3.2 that at low exposures the desorption signal grows proportionally with increasing exposure, but at larger exposures the desorption peak grows more slowly. To better understand this trend, the area under each desorption peak was integrated and these are plotted in Figure 3.3. The desorption signal for sample 72501 grows proportionally up through 256 L exposure, then grows only slightly from 256 to 512 L. This is interpreted as saturation of the chemisorption sites at about 512 L. This saturation value will be used in section 3.3.2 to estimate the concentration of chemisorption sites on the surface of sample 72501.

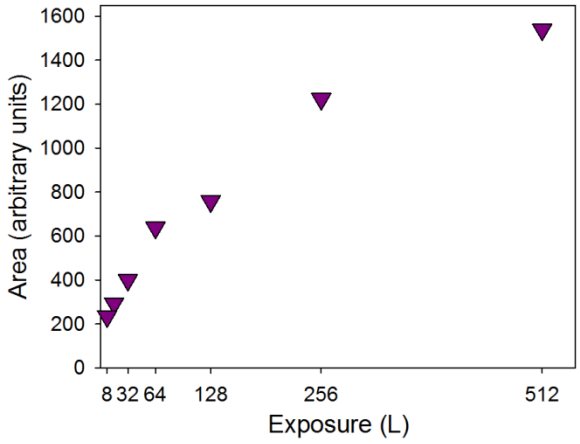

Figure 3.3: Integrated areas under TPD spectra for sample 72501. Chemisorption on the sample surface is approaching saturation when the points begin to level off with increasing exposure quantity.

TPD experiments of lunar sample 12001 exposed to water at 165 K are shown in Figure 3.4. For 12001, water exposures at 110 K resulted in nearly zero discernable chemisorption signal, so dosing above ice desorption temperature was absolutely essential. Exposures on sample 12001 varied from 1 L up to 16 L. Upon heating, adsorbed water began to desorb after the dosing temperature of 165 K, peaked at about 180 K, and returned to baseline around 200 K. There appears to be a broad signal from 230 to 450 K, however, this is not significantly above the baseline and may be a systematic artifact from the blank subtraction process. Water exposure at 250 K produced no peaks in subsequent TPD. The tail at about 500 K is what remains of the signal associated with the heater after the heater subtraction process. The presence of the tail even after the heater subtraction process indicates that the signal from the sample is barely above the noise of the experiment for 12001.

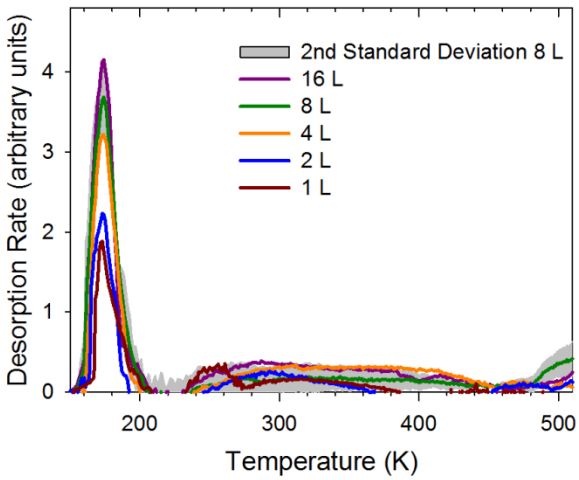

Figure 3.4: TPD spectra for water dosed on the sub-90 µm fraction of Apollo lunar soil sample 12001 at 165 K. Data have been corrected for both heater and blank contributions. Gray shading is the 2nd standard deviation of 8 L exposure on three different days.

The area under each desorption peak for 12001 was integrated and the results are plotted in Figure 3.5, similar to what was done for sample 72501. The integrated area for 12001 grows proportionally up to 4 L exposure, grows slightly between 4 and 8 L, and does not grow significantly from 8 to 16 L. This is interpreted as evidence of saturation of available chemisorption sites at about 8 L exposure. This saturation values will be used in section 3.3.2 to estimate the concentration of chemisorption sites on the surface of sample 12001.

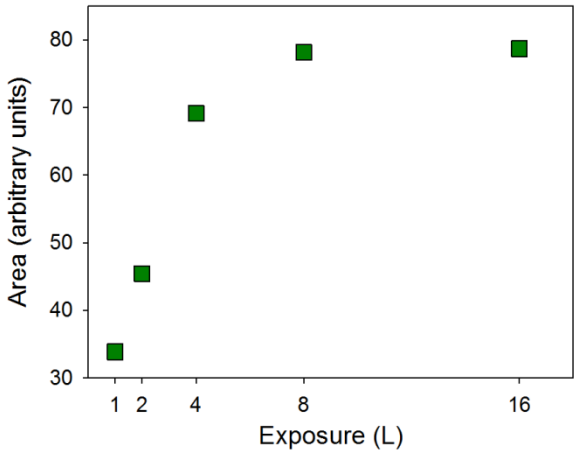

Figure 3.5: Integrated areas under TPD spectra for sample 12001. Chemisorption on the sample surface is approaching saturation when the points begin to level off with increasing exposure quantity.

3.3.2 Energetics and Abundance of Water Chemisorption Sites

Analysis of the distribution of adsorption sites for each sample was carried out by the same method as was implemented previously for lunar surrogate powders by *Poston et al.* [2013] (see section 2.3.5). The method is based on an iterative simulation approach to mathematical ill-posed problems as described by *Barrie* [2008]. The result is a distribution function: the relative abundance of sites as a function of desorption activation energy. Briefly, the method involves: 1) approximating the distribution function by the condensation approximation, 2) simulating the TPD that would be expected from this distribution function, 3) calculating *z* - the residual sum of squares (*rss*) plus a penalty function (*p*) for the simulated TPD and the experimental TPD, and 4) systematically varying the distribution function until *z* is minimized. *p* is based on a second derivative and is intended to keep the distribution function smooth. *Z* contains a

factor, λ, which controls the relative importance of the *rss* versus *p*. λ is chosen by conducting the fitting procedure for multiple λ's and choosing 'by eye' which λ gives the best balance between fit and smoothing.

The distribution function for sample 72501 is shown in Figure 3.6a. Chemisorption sites are seen to extend up to a desorption activation energy of about 1.5 eV. The grey area represents the second standard deviation of three repeat trials. Note that while the mean value shows sites extending to about 1.5 eV, there is less than 95% confidence in the presence of sites above 1.3 eV. The distribution function for sample 12001 is shown with an arbitrary enlargement to make it visible on the graph. The likely reasons for the drastic difference between the two samples will be discussed below.

Converting the distribution function from arbitrary units to units of concentration is possible given knowledge of the total water adsorbed at saturation of the chemisorption sites, the mass of sample used, and the geometric area that the thin film of sample covered on the sample holder. As already mentioned, one Langmuir (L) of exposure represents the statistical expectation of 10^{15} molecules of water arriving at a 1 cm^2 area. Therefore, 1 L represents an exposure to 2.99 x10^{-8} grams of water per cm^2 of geometrical area that the thin film of sample covered on the sample holder. The adsorbed water concentration, *C*, is given by:

$$C = 2.99x10^{-8}\left(\frac{L \cdot a_g}{m}\right)S \qquad (3.1)$$

where *L* is the number of Langmuirs required to achieve apparent saturation, a_g is the geometric area covered by the thin film of sample (in cm^2), *m* is the mass of sample

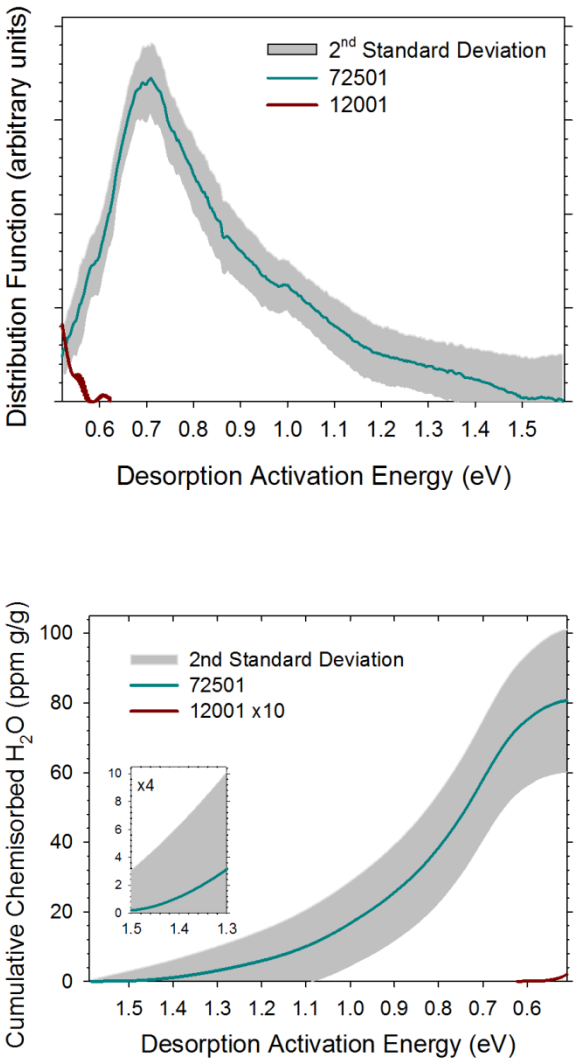

Figure 3.6: Distribution function of desorption activation energies expressed as (a) differential concentration and (b) cumulative concentration from high to low desorption activation energy. Grey shading represents the 2nd standard deviation of three trials for 72501. Inset is four times magnification of the curve from 1.5 to 1.3 eV.

(in g), and *S* is the average sticking coefficient during the water exposure. When the sample is sufficiently cold, *S* can be approximated to be unity, that is, it can be assumed that every molecule impingent upon the sample is retained, either by bonding with the mineral surface (i.e. chemisorption) or by Van der Waals interactions (i.e. physisorption). However, when the temperature is above the desorption temperature of ice, it is unlikely that every molecule incident on the sample will find a vacant chemisorption site before desorbing, i.e. $S < 1$.Such is the case for water exposure to a sample at 165 K.

The average sticking coefficient for 165 K was determined by comparing the total water desorbed after a given exposure at 165 K to the total water desorbed after the same exposure at 110 K, where *S* was assumed to be unity. This procedure results in an average *S* of 0.042 ± 0.010 for 512 L exposure, where the uncertainty represents the second standard deviation. (It was assumed that the primary sources of error in the 165 K and 110 K trials were of the same relative magnitude, therefore the uncertainty was determined by taking the second standard deviation of three trials at 165 K, then doubling the relative error.) The standard deviation accounts for random errors during each TPD, i.e. for *L* and *S* in equation (3.1). Sources of systematic uncertainty for each powder, estimated at 95% confidence, include *m* ± 10% and *a* ± 10%. Inserting all values into equation (3.1) and propagating their uncertainties results in the concentration of chemisorbed water from a 512 L exposure on sample 72501 of 28 ± 5 ppm (g/g).

A similar approach is applied to determine the percentage of the surface, *O*, that is occupied by chemisorbed water molecules at saturation:

$$O = L \cdot S \cdot \frac{a_g}{m \cdot a_s} \tag{3.2}$$

where a_s is the specific surface area of the sample. A typical specific surface area for lunar soil (particles less than 1 cm diameter) is 0.5 ± 0.1 m^2/g [*Cadenhead et al.*, 1977; *Heiken et al.*, 1991], however, only the < 90 μm fraction was used here. Half of the particles, by mass, were retained by the 90 μm sieve, but the largest particles will contribute very little to the specific surface area [*Dyar et al.*, 2010]. Thus it is assumed that a_s is 1 ± 0.2 m^2/g. For sample 72501, using these values in equation (3.2) results in 9 ± 2% of the surface occupied by chemisorbed water molecules at saturation.

Performing a similar analysis for sample 12001 is not possible, due to the difference between the sample analysis and the blank being below the noise of the experiment conducted at 110 K. However, some limits can be set. The upper limit corresponds to $S = 1$ and yields a chemisorbed water concentration of 8 ppm (g/g) and surface occupancy of 3%. A lower limit can be set by taking the exposure at 110 K without subtracting the blank exposure; this results in $S \approx 0.05$ and a chemisorbed water concentration of 0.4 ppm and surface occupancy of 0.1%. A probable result can be obtained by assuming the amount of water adsorbed by an 8 L exposure on sample 72501 at 110 K will be the same as on 12001. This results in $S \approx 0.24$, a chemisorbed water concentration of ~ 2 ppm, and a surface occupancy of 0.7%. While the range set here varies by a factor of 20, the difference is only significant in locations that do not exceed ~ 200 K, because the low desorption activation energies observed for 12001 (see Figure 6a) will retain water only slightly better than physisorption.

The water concentrations derived above correspond to the area under the distribution function for each sample, however, knowledge of the spacing between data points is necessary for interpreting this result quantitatively. A more intuitive way of

expressing the data, which can be read quantitatively, is obtained by integrating the differential distribution function stepwise from highest desorption activation energy to lowest and assigning the total area as equal to the water concentrations derived above. The result of this process is the cumulative distribution function shown in Figure 3.6b, where the concentration read off the vertical axis corresponds to the abundance of water adsorbed at sites of equal or higher desorption activation energy as the corresponding value read off of the horizontal axis.

Sample 72501 clearly has much greater ability to adsorb and retain water than sample 12001. This was expected before-hand for reasons based on mineralogy, maturity index, and probability of contamination prior to sampling on the Moon. Specifically: 1) observations of the 2.95 μm absorption band, which is associated with water molecules adsorbed on silicate minerals, by experiments on three different spacecraft all saw greater 2.95 μm band depth on highlands locations than on the mare; 2) samples of greater ferromagnetic resonance (FMR) surface exposure index, I_S/FeO [*Morris*, 1978], have undergone more weathering and are expected to possess more surface defects than less mature samples, which should lead to more water chemisorption; and 3) sample 12001 was collected near the lunar module at the end of a multi-hour extra-vehicular activity by the astronauts, so it would have been exposed to propellant during landing as well as gas emissions from the equipment and humans between landing and collection, while 72501 was collected over six kilometers away from the lunar module and should be substantially less contaminated. However, perhaps most relevant is the fact that the ALSRC container holding sample 12001 was

found to contain about 5 x10^{-2} torr of gas pressure upon arrival at the storage facility. This pressure of gas (whether trapped astronaut emissions during collection or lunar module or Earth atmosphere leaked in after sealing the box) would certainly contain water and oxygen in sufficient quantity to, if given enough time, react with and permanently heal many of the defects responsible for water chemisorption. Each of these variables predicted greater water chemisorption on 72501 than 12001, but the relative contribution from each cannot be discerned from just these two samples. The contamination of 12001 by gas in the ALSRC container is likely the dominant source of the difference between the two samples.

3.4 Water Persistence on the Moon

The TPD results shown above indicate water retention on experimental timescales (minutes) at temperatures up to 550 K for sample 72501; significantly higher than the maximum temperature experienced on the lunar surface. However, desorption probability is governed by the Polanyi-Wigner equation, which depends exponentially on temperature. Therefore, even for a high desorption activation energy, there is always some probability of desorption. Whether this probability is significant or not is a matter of timescale, i.e. a probability for desorption that is insignificant on the order of minutes may be quite significant on the order of a lunar day (~350 hours of sunlight).

Poston et al. [2013] (see section 2.4) simulated water desorption from lunar surrogates on timescales relevant to the Moon using the distribution function of desorption activation energies and the Polanyi-Wigner equation. Each desorption activation energy was considered separately, though in reality they likely interact, which

may increase desorption losses. The simulation assumes a saturated lunar soil at dawn and tracks only water molecules that never desorb through the lunar temperature cycle. This explicitly ignores any and all sources of new water after the simulation begins, such as readsorption of migrating water or water potentially produced by solar wind hydrogen reacting with oxygen in the lunar regolith each day. The calculation also neglects non-thermal loss processes, such as photon, electron, and ion-induced desorption. Effectively, the simulation produces a TPD in a perfect vacuum chamber and a temperature program matching the lunar temperature cycle for a given latitude.

Water concentrations persisting on a soil of distribution function similar to that found above for 72501 through the temperature cycle of a lunar day for several lunar latitudes are shown in Figure 3.7. All latitudes begin losing water at dawn and continue losing water until after the temperature peaks in the early afternoon. The simulation shows ~ 0.3 ppm of chemisorbed water at 30 degrees, ~1.7 ppm at 60 degrees, and ~ 15 ppm near the pole. The simulation result is in general agreement with the daily trend implied by the spacecraft-based infrared observations, showing decreasing 2.95 μm band depth throughout the morning. However, the simulation results in water concentrations at the low end of the abundances reported from the spacecraft-based data, possibly because the spacecraft are mapping primarily internal water or chemisorbed OH, and not chemisorbed molecular H_2O that is explored here. Internal water (H_2O) has been observed in H^+ irradiated minerals and interplanetary dust particles [*Bradley et al.*, 2014] and hydration of unknown molecular form has been observed in some lunar samples (eg. *Saal et al.* [2008]). Any internal water within the first few micrometers of a grain surface will contribute to a band in the 3-micron region, depth.

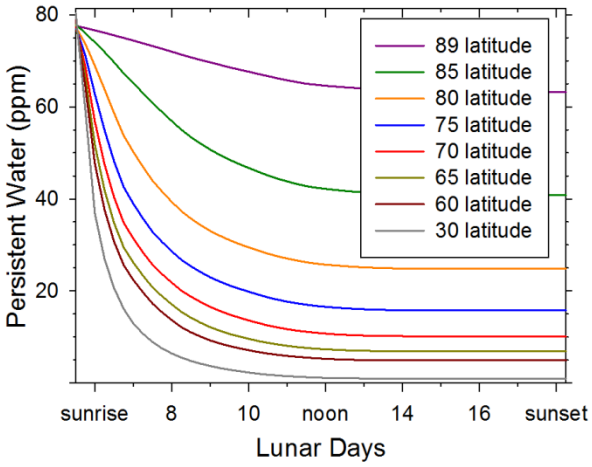

Figure 3.7: Simulation estimating the persistence of chemisorbed water on sample 72501 for one lunar day after a nighttime saturation event. The calculation considers only water that never desorbs and neglects non-thermal loss processes. The simulation uses the estimated sticking parameter from section 3.2.2 for its initial condition.

Therefore, higher water (or OH) abundances should be seen on the Moon than in the simulation of adsorbed molecular water, because the lunar signals will be the sum of internal and adsorbed species, including OH as well as molecular water. A second factor that would increase the observed band depth relative to the simulation here is readsorption of migrating or freshly produced molecular water, which would significantly increase the adsorbed water in the late morning, afternoon, and evening, but not around noon, where the soil is too hot for additional water to adsorb.

The calculation in this section approximates the Moon as a perfectly smooth sphere, and is not valid for PSR's. However, the concepts discussed here can inform interpretations of water stability at the polar regions. Predictions of water-ice stability from Diviner thermal data [*Paige*, 2010] are not always in agreement with observed

neutron-depletion regions (interpreted as hydration of unknown form) [*Lawrence et al.*, 2006; *Mitrofanov*, 2010] or maps of adsorbed hydration from the Lyman Alpha Mapping Project in the ultra-violet region of the spectrum [*Hendrix*, 2012]. Adjusting predictions of hydration and water at the poles to account for chemisorbed water has the potential to improve agreement with these datasets.

3.5 Conclusions

The desorption activation energies for water molecules chemisorbed to Apollo lunar samples 72501 and 12001 were determined by TPD experiments in ultra-high vacuum. A significant difference in both the energies and abundance of chemisorption sites was observed, with 72501 retaining up to 40 times more water (by mass) and with much stronger interactions, possibly approaching 1.5 eV. The dramatic difference between the samples may be due to differences in mineralogy, surface exposure age, and contamination of sample 12001 with oxygen and water vapor before it arrived at the lunar sample storage facility. The distribution function of water desorption activation energies for sample 72501 was used as an initial condition to mathematically simulate a TPD experiment with the temperature program matching the lunar day. The resulting abundances of water persisting through a lunar temperature cycle are in general agreement with spacecraft-based observations of trends in the 2.95 μm absorption band, however, inclusion of internal water and readsorption/production of water throughout the lunar day should improve the match to the lunar observations.

The relatively high temperature of water desorption, 550 K, observed in these experiments is important for a reason not addressed above. According to *Henderson* [2002] in every case where water desorption was observed above 350 K in the laboratory and the surface state of the water was examined by in situ techniques that can discern water from hydroxyl, the surface state was found to be hydroxyl. If the surface state of any water chemisorbed with high desorption activation energy (above ~ 1.2 eV) is hydroxyl and not water, this not only could shift 2.95 μm band depth to 2.8 μm, but would also then have implications for the possible diurnal variation of the 2.8 μm absorption band. Investigations into the surface state of strongly-bound water on lunar samples are thus of high importance.

CHAPTER 4

Experimental Design: Ultra-High Vacuum system for Simulation of Solar Wind Processes on Earth's Moon and other Rocky Solar System Bodies

4.1 Introduction

The idea that solar wind hydrogen (H^+) can react with lunar soil to produce hydroxyl (OH) and possibly water (H_2O) dates back to the early years of planetary exploration and the direct measurement of the solar wind by NASA (e.g. [*Neugebauer and Snyder*, 1962; *Zeller et al.*, 1966; *Housley et al.*, 1974; *Arnold*, 1979]). Laboratory experiments of ion irradiation showing the production of OH within terrestrial glasses and minerals [*Zeller et al.*, 1966] and on lunar samples [*Ichimura et al.*, 2012] have been performed by many investigators, some with negative results [*Burke et al.*, 2011]. Some irradiation experiments have shown possible production of H_2O [*Managadze et al.*, 2011; *Bradley et al.*, 2014] on terrestrial samples.

Recent spacecraft-based observations and laboratory examinations of lunar samples, described in section 1.1 have renewed interest in production of OH and possibly H_2O from the solar wind. One of the most intriguing observations is an apparent diurnal variation in the OH and H_2O concentrations on the Moon [*Clark*, 2009; *Sunshine et al.*, 2009] showing higher band depth at both wavelengths near the day-night terminator, although it is possible it is an artifact of viewing geometry [*Clark*]. This feature, which is tentatively supported by observations from neutron data [*Livengood et*

al., 2014], is difficult to explain without a diurnal source of hydroxyl and water, such as reaction of solar wind H^+ with lunar regolith oxygen.

In addition to formation of hydroxyl and possibly water, solar wind proton irradiation has effects on the physical nature of the lunar regolith surfaces. These effects cause well-documented changes, termed 'space weathering', in the properties of near-infrared reflectance spectra of the Moon (as well as Mercury, Vesta, and asteroids), including 'reddening' and 'darkening' [*Bennett et al.*, 2013]. An as of yet unexplored aspect of space weathering is its effect on water chemisorption. Irradiation of a surface is expected to create defects, which are prime locations for chemisorption. Chapter 3 investigated two samples of lunar material that have experienced different degrees of space weathering, as measured by their I_s/FeO exposure index [*Morris*, 1978]. However, there are a number of other variables involved in the lunar samples, such as mineralogical composition and mode, contamination during collection, transport, and storage, and sources of weathering other than the solar wind (i.e. meteorite impacts, cosmic rays). Separating the contributions of many of these variables is possible by running TPD experiments on a carefully selected set of lunar samples, but the relative effects of different sources of weathering cannot be ascertained by this approach. An ultra-high vacuum (UHV) chamber has been constructed to expose samples to individual weathering agents and measure the effects each agent has on the materials, and to test possible mechanisms of water formation during weathering. A unique aspect of this chamber is the ability to bombard a sample simultaneously with both electrons and ions. Since there are likely to be collective effects, this simulates the solar wind

interaction in a more realistic way. At the time of this writing, the chamber is nearing full functionality. This chapter will describe the design of the chamber and instrument suite that will be applied to these two investigations.

4.2 Description of the UHV Chamber

The space weathering chamber is illustrated schematically in Figure 4.1. The chamber is built on a custom 6-way cross that was available in the lab and has a suitable geometric configuration for the intended examinations. All flange connections in the UHV region are CF-type, i.e. knife-edge into copper gasket design. The main tube is standard size for 6" CF, with 4.5" ports orthogonal to the main tube and 2.75" ports orthogonal to both sets of other ports. A pair of additional 2.75" ports is present in the plane containing the 6" and 4.5" ports, at an angle of 45 degrees to either side of one of the 4.5" ports. This allows three pieces of instrumentation line-of-sight (LoS) to a sample mounted at the focal point of all eight ports, one orthogonal to the sample and two at a 45 degree incidence angle.

A time-of-flight mass spectrometer (TOF) is mounted on a linear translator in the orthogonal LoS position, and an ion source ('ion gun') and an electron source ('e-gun') are mounted in the 45-degree LoS positions. The e-gun is also mounted with a linear translator. A quadrapole mass spectrometer (QMS) is mounted on one of the 6" ports and a6" CF 4-way cross is attached to the other 6" port. This 4-way cross contains the main 230 L/s turbo-molecular drag pump, an ion gauge, and a leak valve for introducing gases to the sample. A Faraday cup is mounted on a rotation post and a linear translator

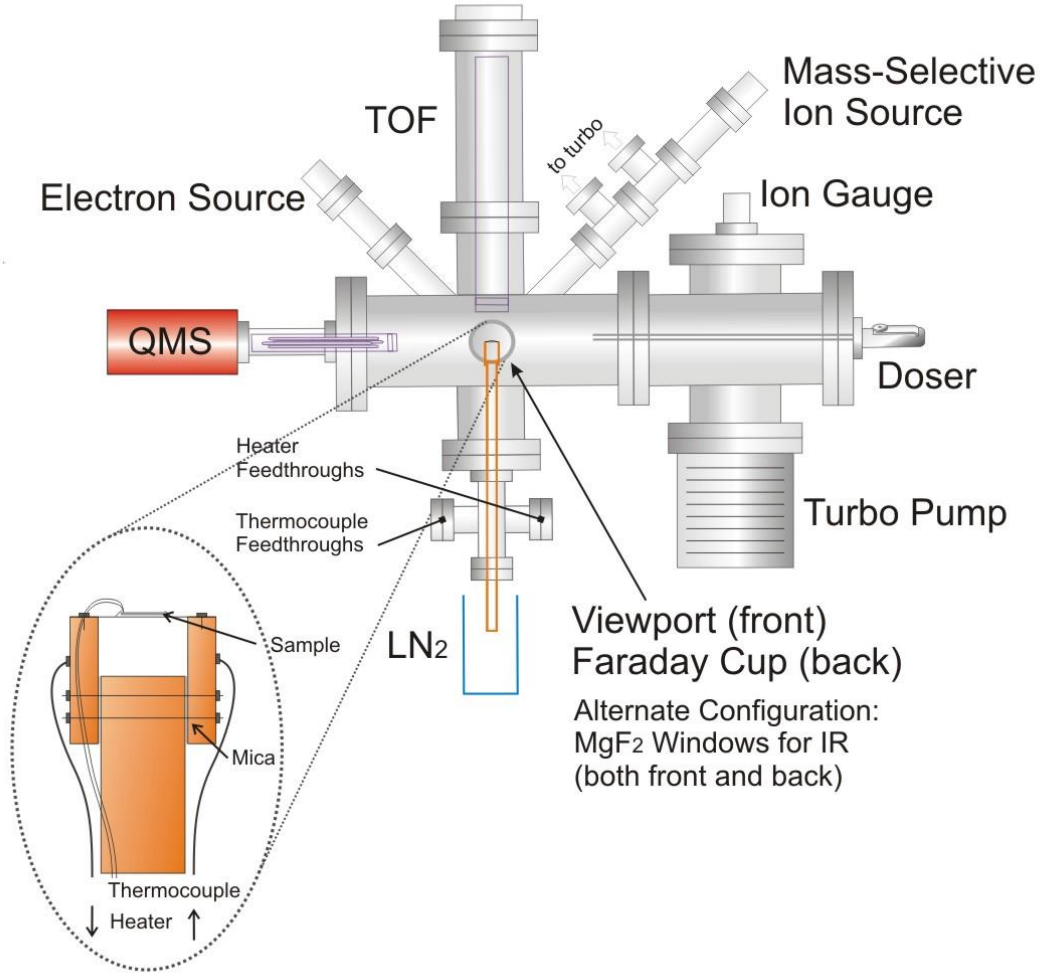

Figure 4.1: Schematic illustration of the ultra-high vacuum system described in this chapter, including close-up view of sample holder (lower left).

on one of the three remaining ports on the main cross, a 2.75”, and a glass window is mounted on the opposite port for viewing the sample and the movable parts.

A second mode is planned where the Faraday cup and glass window are removed and replaced with MgF_2 windows to transmit infrared for grazing angle infrared reflectance experiments. All parts mentioned above are installed and tested except the infrared. The final port on the main cross, the bottom 4.5” port, is used to mount the sample holder, which is currently being optimized for the desired cooling and heating capabilities.

The sample holder (see Figure 4.2) is designed to cool thin slabs of glass, mineral, or lunar rock section to 110 K and heat to 800 K. The sample holder is mounted on the chamber from below, so a high thermal conductivity feedthrough was needed. A 3 kilovolt/600 amp feedthrough from MDC Vacuum is basically an electrically isolated 0.75” diameter copper rod and has the desired high thermal conductivity. This is used as a simple cooling mount. (Note: to reduce risk of shock, the cooling feedthrough must be grounded to the chamber during irradiation.) The thermal feedthrough is mounted through a 5-way cross, with the three additional ports used for a 16 amp heater wire feedthrough and two, dual type-k thermocouple feedthroughs. An extension was machined for each end of the cooling rod: one for the outside that lengthens the rod for submersion in a tall dewar of liquid nitrogen (LN_2) and the other extension for the inside to position the sample at the focal point of the chamber.

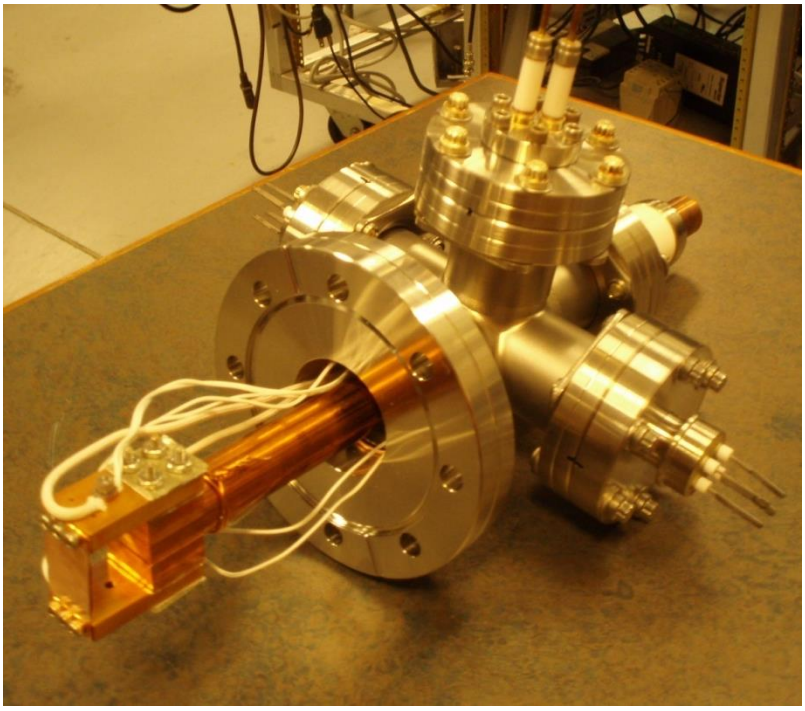

Figure 4.2: Image of the sample holder assembly, shown here with copper jumper for testing purposes.

The rod terminates inside the chamber with the assembly shown in Figure 4.2. The assembly was inspired by a design by *Dawley* [2013] and adapted from a vertical-from-above orientation to the horizontal-from-below orientation shown here. At the very top, a tantalum foil is mounted to span the space between the two outer copper plates, and the sample is mounted on the tantalum foil. The outer copper plates are electrically isolated from the main cooling stage and connected to a power supply so current will flow through the tantalum foil, heating it resistively and transferring heat to the sample by direct contact. The key element is to balance the thermal conductivity of the tantalum foil so that the sample reaches 110 K, while maintaining a sufficient resistance in the foil to provide heating with a reasonable current (a few amps). This approach also

minimizes heat transfer to the cooling stage itself so that it stays below ice desorption temperature and does not become a source of background water peaks in temperature programmed desorption experiments. This optimization process is in progress at the time of this writing.

4.3 Conclusions

A capable system for examining the effects of ions and electrons of typical solar wind composition and energy on lunar surrogates and genuine lunar samples has been designed, constructed, and is nearing full functionality. This system will enable experimental examination of as-of-yet untested mechanisms for possible formation of water on rocky, airless solar system bodies, such as Earth's moon. It will also be used to examine the effects of active irradiation and defect production on the adsorption and dissociation of water. Both of these investigations are essential to understanding data returned by spacecraft-based investigations and the sources, evolution, and eventual fate of water on Earth's moon.

CHAPTER 5

Production of Hydrogen from Water Adsorbed on Zirconia Nanoparticles Under Irradiation by Ultraviolet Photons

5.1 Introduction

Photo-catalytic splitting of water using corrosion resistant metal-oxide (MO) particles is a topic of wide scientific and technical interest. This is largely due to the current need for advances in alternative energy technologies and the potential role of water splitting in hydrogen (H_2) generation. Though metal-oxides are resistant to corrosion and degradation, MO particle band-gaps are often high and outside the peak wavelength region of the solar spectrum at the surface of Earth. Despite this fact, these types of particles are useful for examining the fundamental mechanisms of water splitting and the relative importance of hot hole and electron transfer vs. the possibility of direct exciton transfer to the interfacial water. A significant amount of previous work examining photo-induced water splitting processes has been reported [*Kudo and Miseki*, 2009]. However, to our knowledge, there are few studies that directly probe the role of excitons and the coverage dependence of the H_2 production probability using MO nanoparticles.

An interesting system that may demonstrate the role of exciton transfer to interfacial water in the photolysis of water involves zirconia (ZrO_2) nanoparticles. Photo-catalytic decomposition of water over ZrO_2 powder was first examined in detail by *Sayama and Arakawa* [1993]. These authors demonstrated that while H_2 evolved from ZrO_2 in pure water under ultraviolet (UV) irradiation, the addition of a carbonate salt

was necessary to also evolve molecular oxygen (with CO as a byproduct) [*Sayama and Arakawa*, 1994; 1996; *Arakawa and Sayama*, 2000]. In contrast to the highly studied titania system [*van de Krol et al.*, 2008; *Kudo and Miseki*, 2009], the addition of a co-catalyst, such as platinum, decreased the H_2 yield. Despite ZrO_2's ability to produce H_2 from water without any co-catalyst, much less attention has been given to this simple photo-catalyst largely because the large bandgap of ZrO_2 (~5 eV) prohibits its use as an efficient solar photo-catalyst.

ZrO_2 is also a typical component of nuclear fuel rod cladding materials. If adsorbed water is present, these surfaces can stimulate the formation of H_2, especially under high temperature and radiation bombardment conditions. *Petrik et al.* [2001] surveyed 30 bare oxide powders, including ZrO_2, for conversion of water into H_2 under gamma irradiation (1.25 MeV). They compared H_2 production to the literature bandgap values for the oxides and observed a peak in H_2 production at bandgaps of about 5 eV. This is well below the 6.6 eV transition energy required to dissociate gas-phase water via the first excited state [*Henderson*, 2002]. Petrik et al. interpreted the 5 eV bandgap value as indirect evidence of an energy-transfer mechanism involving fundamental excitons. These are usually located at an energy slightly below the material band-gap edge. *LaVerne* [2005] measured H_2 yields during gamma irradiation of two phases of ZrO_2 nanoparticles suspended in water. He found that the efficiency of H_2 production was higher on the tetragonal phase than on the monoclinic phase. *Roth et al.* [2012] examined H_2 production from water adsorbed to an unidentified phase of ~350 nm diameter ZrO_2 particles after gamma, He^+, and fast electron irradiation. They concluded

that H_2 production occurred within the first monolayer of adsorbed H_2O and is not from decomposition of surface OH groups.

Reddy et al. [2003] examined the effects of varying the hydrolyzing agent in ZrO_2 synthesis by the precipitation method. The efficiency of hydrogen evolution for these nanoparticles under UV irradiation from a high pressure Hg lamp was about a factor of two higher for samples containing 56% monoclinic phase particles than for the nanoparticles of 95% monoclinic phase. Band edges for these nanoparticles were stated to be 315 nm (3.93 eV), well below the normal ZrO_2 band gap of 5 eV. Thus, the hydrolyzing agent and general synthetic process significantly alters the defect types, densities and surface electronic structures.

In this chapter, systematic studies of H_2 yields after photoirradiation of thin, adsorbed layers of water on monoclinic and cubic phase nanoparticle ZrO_2 surfaces are reported. Specifically, we examine the dependence of H_2 production rate from water adsorbed on ZrO_2 nanoparticles as a function of 1) ZrO_2 crystal phase (monoclinic and cubic), 2) photoexciation above and below the bandgap (185 nm /6.7 eV and 254 nm/4.9 eV, respectively), and 3) water coverage (0 to 5 monolayers). The results show formation of H_2 is efficient on a per-absorption basis, occurs primarily over the bilayer regime and strongly depends upon the crystal phase of the nanoparticles. This can be interpreted in terms of effective exciton transfer to the adsorbed interfacial water molecules for monoclinic phase particles vs. self-trapping within or on the more defective cubic nanoparticles.

5.2 Experimental Methods

5.2.1 Description of the Samples

The nanoparticle suspensions ranged from pure cubic to pure monoclinic phase. All samples were produced from the same starting reagents. Monoclinic ZrO_2 nanoparticles were prepared by the hydrothermal method [*Yoshimura and Somiya*, 1999; *Bondioli et al.*, 2001; *Han*, 2008] from aqueous solutions of $ZrCl_4$ (Alfa Aesar, 99.5+%) and NaOH (EMD, ACS grade). Cubic phase ZrO_2 nanoparticles were prepared by the hydroxide method [*Petrunin et al.*, 2004] from the same solutions. Mixed phase samples were prepared by the same synthesis as the monoclinic samples, but the time and temperature of annealing were varied to control the phase distribution. The product was a fine white powder with particle diameters ranging from 15 nm to 60 nm.

5.2.2 Instruments for Characterization of the Samples

X-ray diffraction data (XRD) was collected with a Bruker D8 ADVANCE X-ray diffractometer over a 15º – 85º 2θ range. Particle sizes were determined from the average peak broadening of the four strongest Bragg peaks using the commercial program TOPAS. UV absorption spectra of each phase were collected with a Varian Cary 5E with a diffuse reflectance accessory and 1 µm diameter polytetrafluoroethylene (PTFE) powder (Aldrich) as a reference. Surface areas were determined by the BET method [*Brunauer et al.*, 1938] using Micromeritics software and a Micromeritics Tristar 3000, with nitrogen as the adsorbent. The total surface area of each sample varied from 1 to 5 m^2. H_2 evolution was normalized to the total ZrO_2 surface area in each experiment and did not depend directly on nanoparticle size in the range studied.

5.2.3 Vacuum System for Water Photolysis with Ultraviolet Photons

The apparatus used to quantify the H_2 yield from water photolysis on ZrO_2 particles is shown in Figure 5.1. The apparatus consists mainly of a gas handling system and a quartz photolysis cell that is coupled to a differentially pumped quadrapole mass spectrometer. ZrO_2 powders were placed on the flat, quartz window (diameter 10 mm) of the photolysis cell and irradiated with UV light (254 or 185+254 nm) from one of two low pressure mercury discharge lamps

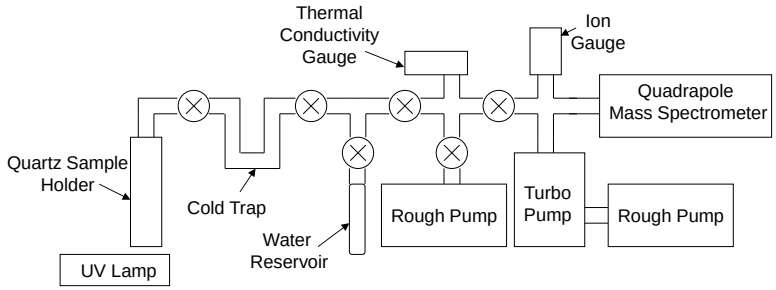

Figure 5.1: Schematic of the water photolysis apparatus used to quantify the efficiency of zirconia nanoparticles for H_2 production.

(PenRay mod. 11SC-1). The two lamps were identical except for a coating on one of the lamps that absorbs photons with wavelengths shorter than 200 nm (i.e. energy >6.2 eV). Photometry measurements comparing the intensity at 185 nm (6.7 eV) between the two lamps show that >99% of 185 nm photons are absorbed by this coating. Thus, the coated lamp emitted only 254 nm whereas the uncoated lamp emitted both 254 and 185 nm photons, with typical total fluxes ~ 10^{16} s^{-1}.

Prior to irradiation, ZrO_2 samples were heated to 500 K under a 10^{-3} torr vacuum to remove adsorbed substances (mostly H_2O and CO_2 boundas a carbonate-like species).

Next the sample was cooled to room temperature and irradiated in a closed volume to establish a baseline response of the system. Following the baseline, water vapor was supplied at 300 K such that the equilibrium surface coverage was in the desired range from 0.001 to 5 monolayers [*Holmes et al.*, 1974]. After subsequent irradiation, water was trapped on the sample by freezing in liquid nitrogen. The residual gas (H_2 with traces of CO, CO_2, H_2O, and N_2) was released into a fixed volume (~65 cm^3) and the pressure was measured with a thermal conductivity gauge. Finally, the gas was analyzed by a differentially pumped Pfeiffer Prisma 80 quadrapole mass spectrometer.

5.3 Results

5.3.1 Physical Characterization

Typical XRD data are shown in Figure 5.2 and a TEM image showing the typical size distribution of the nanoparticles is shown in Figure 5.3. The powders are identified as monoclinic and cubic crystalline phases based on the XRD peak positions and magnitudes. (Note that the XRD pattern for a third common phase of ZrO_2, tetragonal, is very similar to cubic, however, they differ in that the peaks split for tetragonal phase particles, but do not split for cubic phase particles.) The fraction of monoclinic phase was calculated from the peak area of the primary monoclinic peaks over the sum of the peak areas of the primary monoclinic peaks and the primary cubic peak [*Chang and Doong*, 2005].

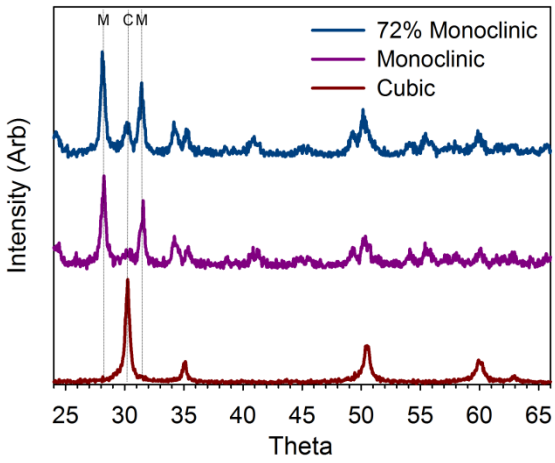

Figure 5.2: XRD patterns from end member nanoparticles and one intermediate phase. The primary monoclinic peaks are marked with “M” and the primary cubic peak is marked with “C”.

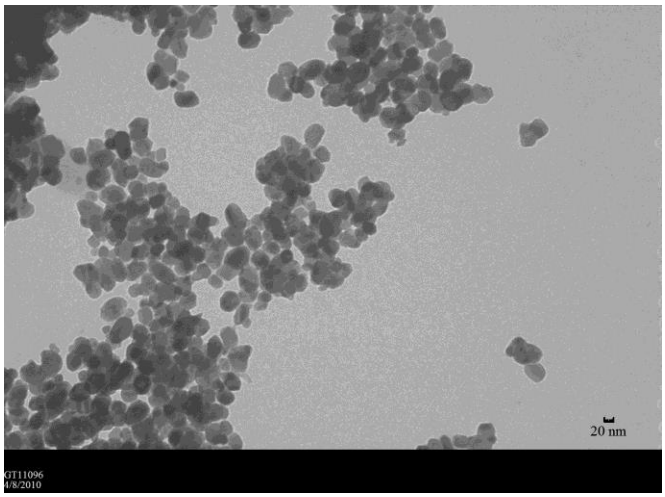

Figure 5.3: TEM image of typical ZrO_2 nanoparticles from this experiment.

5.3.2 Hydrogen Produced by Phase and Photon Energy

The amount of H_2 produced over ZrO_2 mixed-phase nanoparticles as a function of the fraction of monoclinic phase is presented in Figure 5.4. (Note that no oxygen

production in amounts close to stoichiometric was detected). These data show that the rate of H_2 production in the presence of pure monoclinic ZrO_2 is more than an order of magnitude greater than in the presence of pure cubic phase. In the case of mixed-phase powders, the rate of H_2 evolution increases with the fraction of monoclinic phase. H_2 evolution was normalized to the total ZrO_2 surface area in each experiment and did not depend directly on nanoparticle size in the range studied. The input from water photolysis in the vapor phase above the sample was also measured to be negligible.

A second significant result presented in Figure 5.4 is the strong dependence of water photolysis rate with photon energy (note the different left and right axis labels). The use of a lamp that emits both 254 and 185 nm photons results in an order of magnitude increase in H_2 production when compared to the coated lamp, which passes primarily 254 nm photons. Therefore, while the 185 nm photons are only about 3% of the total

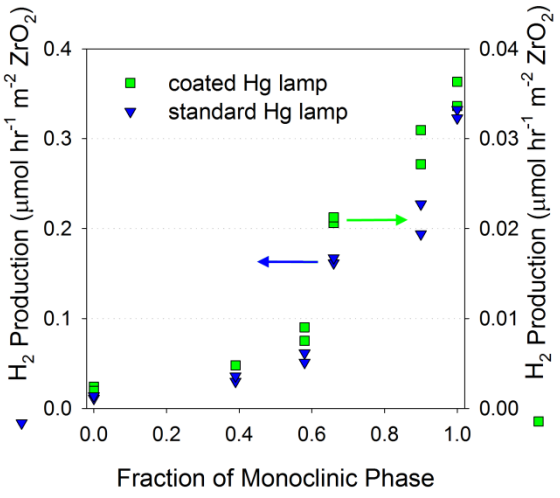

Figure 5.4: The amount of H_2 produced over ZrO_2 mixed-phase nanocrystals with different monoclinic to cubic phase ratio under UV light irradiation using both 185 and 254 nm (blue triangles) and only 254 nm (green squares) photons. Note the different scales for each lamp. Water coverage is ~ 3 layers.

flux using the standard lamp, they dominate the water photolysis. Though the yields are substantially less using only 254 nm, the variation in photolysis rate with crystal phase is similar in both irradiation environments. The similar behavior of these nanoparticles implies a mechanism that involves absorption of photons by the nanoparticles, followed by energy migration to the surface. Since 254 nm is not above the gap energy, the likely energy carrier is an exciton.

5.3.3 Band Gap and Relative Defect Concentration by Ultraviolet Diffuse Reflectance Spectroscopy

In order to understand the influence of the ZrO_2 nanoparticle crystal structures on the photolysis efficiency, we must first characterize the electronic structure. Diffuse reflection of ZrO_2 powders was measured in the range 200-350 nm (relative to powdered PTFE) and converted into absorption (see Figure 5.5). The region excited by

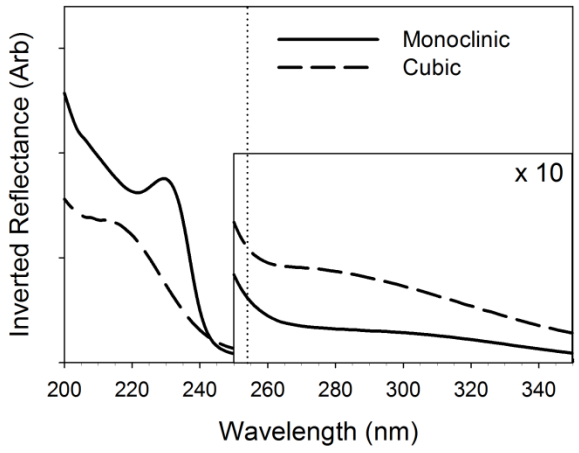

Figure 5.5: UV diffuse reflectance spectra of monoclinic (solid) and cubic (dashed), ZrO_2 nanopowders. The vertical dotted line at 254 nm indicates wavelength of incident photons.

the 254 nm (4.9 eV) photons is shown by the dotted line and is right before the onset of the main band-edge absorption (i.e. the band gap, E_g energy) of both the monoclinic and cubic crystals. It is well known that the wavelength of the edge of fundamental optical absorption of ZrO_2 depends on crystal structure [*French et al.*, 1994]. Further, it is known [*Ciuparu et al.*, 2000; *Navio et al.*, 2001; *Yuan et al.*, 2008] that defects will cause absorption tails well into the band gap, which could cause differing absorption of 4.9 eV photons between phases. Indeed the data in Figure 5 are consistent with this. The shallow slope to the band edge and the greater absorption in the defect tail for the cubic phase ZrO_2 indicate a greater defect density in this phase.

5.3.4 Water Coverage-Dependence Measurements

The experimental dependence of H_2 evolution rate on surface coverage of water in the range 0.001 - 5 monolayers (ML) was also examined with the standard Hg lamp and is presented in Figure 5.6. It shows direct proportionality of the reaction rate with water coverage for values less than 0.01 ML. At 0.01-1 ML coverage a non-linear increase of the reaction rate is observed. Further increase in the reaction rate with coverage above 1 ML layer is slow, indicating energy transfer only to water molecules of the first layer. The maximal rate of water photolysis is observed at coverage about 2-4 ML.

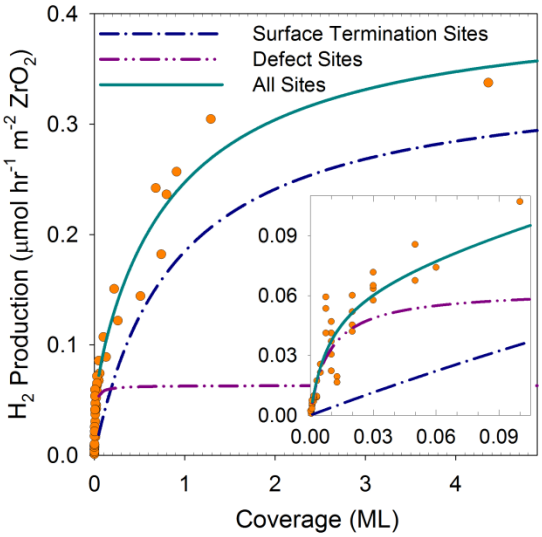

Figure 5.6: The amount of H_2 produced by irradiation (185 + 254 nm) of monoclinic phase ZrO_2 nanoparticles with different water surface coverage. The dashed lines represent the rates of formation/ dissociation of adsorption-complexes associated with defect sites or surface termination sites (purple and blue, respectively). The solid line (teal) represents their superposition. Inset is an enlarged view of the low coverage experiments.

5.4 Discussion

5.4.1 Electronic Structure and Hydrogen Production Mechanism

The overall mechanism we propose here for water photolysis is: 1) Absorption of a 4.9 or 6.7 eV photon in the ZrO_2nanoparticle to form an exciton. 2) Diffusion of the exciton until it is trapped at a surface site with an adsorbed water molecule. 3) Transfer of the energy from the exciton to the water molecule-adsorption complex, and 4) water dissociation into either H + OH or H_2 + O fragments.

The valence band of ZrO_2(both monoclinic and cubic phases) has character derived primarily from the oxygen 2p atomic orbital while the conduction band is primarily

zirconium 4d in character [*French et al.*, 1994; *Kralik et al.*, 1998; *Garcia et al.*, 2006; *Taylor et al.*, 2012; *Zhang et al.*, 2013]. The calculated values of the direct band gap range from 3.6 to 5.8 eV for cubic phase ZrO_2 and from 3.2 to 5.5 for monoclinic phase ZrO_2 [*Kralik et al.*, 1998], while experimentally measured gaps have been reported from 5.0 to 5.8 eV (see *Taylor et al.* [2012] and refs. within). The valence and conduction band density of states are both several eV wide, so excitation by both 4.9 and 6.7 eV photons will result in an excited electron in the conduction band (see *French et al.* [1994]) for width of the VUV absorption peak corresponding to valence → conduction band transitions). Measurements of the onset of optical absorption at about 5 eV reported here (see Figure 5.5) for the ZrO_2nanoparticles are in agreement with theory and previous measurement.

It has been proposed previously [*Petrik et al.*, 2001; *LaVerne*, 2005] that water photolysis on ZrO_2 nanoparticles takes place by a mechanism involving excitons. Excitons are bound by the Coulomb potential energy:

$$V = \frac{-e^2}{rK}, \tag{5.1}$$

where *e* is the charge of an electron, *K* is the relative permittivity (historically termed the dielectric constant), and *r* the distance between the hole and electron (eg. *Band* [2006]). ZrO_2 has a high *K* of ~25 times that of vacuum, which screens the interaction between the hole and the electron, resulting in a value of *r* spanning tens to hundreds of unit cells. Such a delocalized exciton is known as a Wannier-Mott exciton and can be described mathematically in a fashion similar to an H atom in a dielectric medium. Using

this analogy, the unbound level for the exciton is the energy of the band gap, with bound exciton states existing at energies just below the energy of the gap. The binding energy depends on the electron reduced effective mass and the square of K for the material, and for a high dielectric material will typically be less than the thermal energy at room temperature, so diffusion is expected to be significant.

Diffusion can be thought of as a random walk from the origin of the exciton, with the distance an exciton can diffuse governed by the exciton diffusion coefficient and the lifetime before the exciton spontaneously relaxes. Since the exciton must reach the surface in order to transfer its energy to dissociate the water molecule, a high surface-to-volume ratio, such as is found on nanoparticles, will improve the likelihood of this reaction. In principle, the shorter the diffusion distance needed from source to surface trap the better. Neither LaVerne nor control experiments performed in the present study found any direct relationship between particle diameter and efficiency of H_2 production for particles smaller than 110 nm. However; a dependence on surface area was observed in the present study.

The dominant process governing diffusion of excitons to reach the active surface sites appears to be the presence of crystal defect sites within or on the nanoparticles. These defects can react with and annihilate excitons, preventing the energy from reaching and dissociating water molecules at the surface. As was discussed briefly above, one way defects reveal themselves is by creating states within the band gap, which can be seen as absorption of photons at energies below the gap. Such absorption is seen for cubic phase ZrO_2 nanoparticles in Figure 5.4, but much less for monoclinic

phase ZrO_2 nanoparticles. The monoclinic nanoparticles were produced by annealing to a higher temperature than the cubic nanoparticles; it appears that nearly all defects were annealed out of the monoclinic nanoparticles while many remained in the cubic nanoparticles. We conclude the phase-dependence of water photolysis seen on the ZrO_2 nanoparticles (see Figure 5.4) is mainly due to differences in defect density between the two phases of nanoparticles. Excitons that reach the surface are trapped preferentially at surface defects, which are also the most stable location for water molecules to adsorb.

VUV spectra for water in the gas phase follow dipole and Frank-Condon selection rules and show a first excited state transition energy peak maximum of ~7.5 eV and absorption threshold ~6.6 eV (see *Henderson* [2002]). The energy of the H-OH bond in the water molecule is 5.1 eV, (similar to the energy contained by the ZrO_2 exciton) and the first excited state of water is dissociative ($H_2O^* \rightarrow H + OH$). When water adsorbs at an oxygen vacancy (net negative charge) on the ZrO_2 surface, electron density will donate from the defect to the water molecule, partially filling the first available unoccupied levels of the adsorbed water molecule. These levels have $4a_1$ character and are anti-bonding so the strength of the H-OH bond will be reduced and the H-O-H angle will increase. Subsequent excitation by energy transfer from the exciton further reduces the bonding character, resulting in dissociation to form an H atom and adsorbed OH. Free H atoms then react to form H_2, which is the molecule detected in these experiments.

The above process is certainly the most likely result of absorption of photons at 4.9 eV to form H_2, however, in the case of 6.7 eV photons, a second process may be occurring. Measurements of the species formed during scattering of low energy electrons (5-40 eV) in water-ice at 88 K have shown the ejection of neutral H, H_2, and O species [*Kimmel and Orlando*, 1995]. The threshold for formation of all of these fragments is ~6-7 eV. This low threshold energy, as well as observation of non-thermal $O(^3P_J)$and highly vibrationally and rotationally excited H_2 indicated the possible formation of H_2 directly ($H_2O \rightarrow H_2 + O$) by molecular elimination. The channel forming $O(^3P_J)$ is not optically active, because it requires an excited state with triplet character. For this process to occur in the present system, an exciton of triplet character must be produced. For above gap transitions, this is statistically probable via an electron-hole recombination process. Once formed the triplet character must be preserved while diffusing through the ZrO_2nanoparticle and transferred to the adsorbed water molecule. Since we do not detect the $O(^3P^J)$ fragment in this experiment, we cannot determine the relative importance of this channel for above gap photon energies.

5.4.2 Quantum Yield

Several variations of quantum yield can be calculated for the monoclinic phase nanoparticles with a full layer of adsorbed water molecules. In our experimental setup, there were ~$7x10^{13}$ (s^{-1}) H_2 molecules produced and ~$2x10^{16}$ (s^{-1}) photons incident on the powder, ~3% with energy 6.7 eV and the balance 4.9 eV. Simply taking H_2 molecules produced over photons incident produces the apparent total quantum yield of ~$4x10^{-3}$ H_2 molecules per photon incident. The apparent yield for only 4.9 eV photons is an order

of magnitude lower: $4x10^{-4}$ H_2 molecules per photon incident. Separating out the 6.7 eV photons produces an apparent yield of 0.12 H_2 molecules per 6.7 eV photon incident. This large difference in yield is due largely to the difference in absorption of photons by the ZrO_2 between the two energies. When considering only absorbed photons, the quantum yields for photons at both energies are essentially the same. These nearly identical efficiencies indicate that the same mechanism is likely dominant for both photon energies. The quantum yield(s) for the cubic phase ZrO_2 nanoparticles is ~10 to 20 times lower than the monoclinic because the cubic phase particles both absorb a higher fraction of the incident photons at 4.9 eV and produce an order of magnitude less H_2.

5.4.3 Kinetics

The dependence of H_2 yield on the concentration of adsorbed water molecules can be explained in terms of second order kinetics. The observed direct proportionality of H_2 evolution to photon fluence means that during UV irradiation the system exists in a state of dynamic equilibrium where water concentration at the surface effectively does not change over time. Efficient photolysis takes place only within the first adsorbed layer, consistent with an exciton charge-transfer mechanism, and increasing water content from 1 to 5 MLs increased the photolysis rate only about 20-25%. Thus, decomposition occurs only for water molecules in contact with the ZrO_2 surface, i.e. after forming a specific adsorption complex involving a water molecule in the first layer and some regular surface site or structure defect, *D.* The rate of water photolysis depends on parameters such as the photon flux, reaction probability (i.e. photolysis rate

constant) and the concentrations of these specific adsorption complexes. Assuming the adsorption complex is formed by the reversible interaction of a migrating water molecule with a regular site and/or specific surface defect, then the reaction of interest is the following dynamic equilibrium:

$$D + W \leftrightarrow C \tag{5.2}$$

where *D* is a surface defect, *W* is a water molecule, and *C* is a surface complex. The equilibrium concentration, [*C*], can be presented by a standard kinetic equation:

$$\frac{d[C]}{dt} = k_{dir} \times [W] \times ([D_0] - [C]) - k_{inv} \times [C] \tag{5.3}$$

where k_{dir} and k_{inv} are equilibrium constants for formation and dissociation of the adsorption complex, [D_0] is the total concentration of surface sites of this type, and [*W*] and [*C*] represent surface concentrations of water and the surface complex, respectively. The rate of *C* formation is proportional to the water concentration at the surface and the concentration of the available sites, [D_0]-[*C*]. While in equilibrium, rates of the direct and inverse reactions are equal, and the surface concentration of the adsorption complex is:

$$[C] = \frac{{}^{k_{dir}}/_{k_{inv}} \times [D_0] \times [W]}{1 + {}^{k_{dir}}/_{k_{inv}} \times [W]} = \frac{k \times [D_0] \times [W]}{1 + k \times [W]} \tag{5.4}$$

where *k* is the equilibrium constant, k_{dir}/k_{inv}. Within the water coverage range studied, the process is satisfactorily described by a superposition of two processes:

$$[C_{total}] \approx [C] + [C'] = \frac{k \times [D_0] \times [W]}{1 + k \times [W]} + \frac{k' \times [D_0'] \times [W]}{1 + k' \times [W]} \tag{5.5}$$

where *k* and *k'* are the equilibrium constants for the formation and dissociation of two types of adsorption complexes, [D_0] and [D'_0] are initial concentrations of surface

defects of two different types, which react with water molecules, *W,* to form photo-active adsorption complexes *C* and *C'*, and [C_{total}] represents the surface concentration of all photolysis-reactive surface complexes.

The first term in equation 5.5 (purple, double-dot-dashed line in Figure 5.6) fits the data well for water coverages from 0.0005 to approximately 0.06 ML. The contribution of the second term (blue, dot-dashed line on Figure 5.6) is negligible over this coverage regime. At low coverage, water mostly adsorbs at the defects of the first type, *D*, probably in a strongly-bonded chemisorbed form. At coverages >0.06 ML, defects of the first type are completely occupied by H_2O molecules and converted into adsorption complexes, C. The concentration of complex C remains constant in spite of its efficient photolysis due to its fast regeneration caused by water re-adsorption on a vacant *D*-site from less strongly bonded forms, including *C'*. H_2 production from the type-*C* complexes reaches the approximately maximum rate at coverage of ~0.06 ML and remains approximately constant at all higher coverages. At coverage greater than ~0.06 ML the second term in equation 5.5 dominates H_2 production, requiring a superposition of the two terms to adequately describe the observed rates. Fitting equation 5.5 to the data resulted in a value of 0.06 ML for surface site D and 0.35 ML for surface site D', i.e. sites D cover ~6% of the surface and sites D' ~35%. The data (Figure 5.6) show that H_2 production rate continues to increase up to a full monolayer, but this is due to the rapid reformation of surface complexes at D' sites. *Roth et al.* [2012] also found evidence for two types of chemisorption sites on their ZrO_2 particles during a temperature program desorption study, while *Petrik et al.* [2001] saw only one.

The apparent saturation of *D*-type sites means that the initial number of such sites, D_0, is not more than ~ 6% of all surface sites available for water adsorption. (Although both sites are treated as defects in the nomenclature above, they do not necessarily both have to be structural defects: one of them is likely a regular surface site). The rate constant k is ~100 times greater than k'. The rates of both direct reactions (k_{dir}) are similar, because they are controlled by water diffusion over the surface. Therefore, the two orders of magnitude difference between *k* and *k'* is, most likely, caused by the rates of the inverse reactions (k_{inv}), i.e. the rates of dissociation back into an unoccupied site and a mobile water molecule. In other words, *C* is much more stable, likely due to a stronger interaction of water with the surface when compared to *C'*.

5.5 Conclusions

The formation of H_2 from photolysis of water adsorbed on zirconia (ZrO_2) nanoparticles under 254 nm (4.9 eV) and 185 nm (6.7 eV) photon irradiation was examined. The H_2 yield was considerably higher using monoclinic versus cubic phase nanoparticles. Monoclinic particles containing 2 ML of water showed a maximum H_2 production rate of ~0.4 μmole hr^{-1} m^{-2} using 185 + 254 nm excitation. This rates drops by an order of magnitude when using near-gap (254 nm) photons. An H_2O coverage-dependence study of the H_2 yield is best fit by a sum of interactions involving at least two types of adsorbate-surface complexes. The first dominates up to ~0.06 ML and is attributed to H_2O chemisorbed at surface defect sites. The second dominates at coverages up to a bilayer. H_2 formation is maximum within this bilayer and likely results from efficient energy transfer from the particle to the interface. Energy transfer is more

efficient for the monoclinic ZrO_2 nanoparticles and likely involves mobile excitons. UV-Vis spectroscopy reveals the cubic phase nanoparticles to contain a greater concentration of crystal defects, which serve as trapping sites where excitons are lost. The detrimental role of defects on the process contradicts a mechanism involving direct absorption of the photons by the water adsorbed at defect sites. The results show the photo-induced water-splitting is primarily a surface-mediated event and the use of nanoparticles is generally beneficial due to enhanced surface-to-volume ratios. In the case of ZrO_2 nanoparticles, exciton transfer to the adsorbed water molecules seems likely.

Conclusions

Water on the Moon and other solar system bodies near Earth carries clues to the formation and habitability history of the solar system and is also useful as a resource to make space exploration more sustainable. Understanding the sources, evolution, and fate of water on these bodies is critical. The main drivers of all water processes on airless, rocky bodies are temperature, meteoroid impacts, and radiation from electrons, ions, and photons; each driver can be a source of water, a stimulus for water evolution, and a means of removing or sequestering water. The work described in this thesis has examined the thermal behavior of water on lunar surrogate materials and genuine lunar samples brought to Earth by the Apollo missions. In addition to the ultra-high vacuum (UHV) system constructed for the TPD experiments, a second UHV system has been designed and is nearly operational for experiments simulating electron, light ion, and photon effects on airless, rocky bodies, and their synergistic effects on water thermal processes. Finally, an examination of water photolysis on zirconia nanoparticles has been conducted to better understand the mechanism of water photo-decomposition to form hydrogen gas on this simple metal oxide – a process which may be relevant both for in situ resource utilization (ISRU) in space and here on Earth for storing solar energy as chemical energy. The conversion of hydrogen using a fuel cell can ultimately lead to an emissions-free energy source that generates power even when the sun is no longer shining.

The thermal behavior of water on lunar materials was investigated by temperature programmed desorption (TPD) experiments in an UHV system designed and constructed

specifically for these investigations. These investigations are critical to the planetary science community because the current means of modeling water migration and retention on the Moon (which transfers to other airless bodies with minor modifications) neglect the direct interactions between the adsorbate water molecules and the mineral substrate. In fact, since water concentrations are very low on the lunar surface, these direct interactions will dominate the water residence times and incorporation of them into models has the potential to significantly change the expected evolution and sequestration of water on the Moon.

Lunar surrogate materials (Chapter 2: mechanically micronized JSC-1A and albite) and lunar soil samples (Chapter 3: samples 72501 and 12001) were found to chemisorb water molecules onto the grain surfaces. Because the samples are heterogeneous powders, they were found to have a single, broad desorption peak during the TPD, which is interpreted as evidence for chemisorption sites with a distribution of desorption activation energies. The distribution function of desorption activation energies was determined for each sample by a custom, iterative simulation program. The surrogate materials were found to possess similarly shaped distribution functions, with the highest energy chemisorption sites detected at about 1.2 eV. Calibration of the water concentration by the apparent saturation of chemisorption sites showed the surrogates to differ in total adsorption by up to a factor of two. The micronized albite possessed greater ability to adsorb water than the micronized JSC-1A, which may indicate a mineralogical effect on adsorption that matches the trend of greater 2.95 μm band depths on highlands relative to mare regions. This trend has been seen by

spacecraft-based observations at the Moon. Both samples were micronized in a similar fashion, which was intended to simulate weathering by impacts on the Moon, so their effective maturity should have been similar, allowing mineralogy to be examined.

The lunar samples were found to have a dramatic difference in ability to chemisorb water molecules. 72501, a soil dominated by highlands material, possessed chemisorption sites with desorption activation energies possibly as strong as 1.5 eV. These higher energy chemisorption sites will retain water much more effectively than the marginally lower desorption activation energy sites detected on the micronized surrogate materials. On the other hand, 12001 chemisorbed water only slightly more effectively than physisorption of ice and significantly less effectively than any of the other three samples. The two lunar samples differed on many variables that are expected to affect water chemisorption: mineralogy, surface maturity from space weathering, and possibility of contamination before collection by the astronauts. It is noteworthy that sample 12001 arrived at the lunar sample laboratory with a 5 $x10^{-2}$ torr gas contamination in its holding vessel. If the sample was exposed to this gas for several days, the gas could react with sample 12001 and passivate the strongest water chemisorption sites. This emphasizes the importance of sampling a significant distance from the landing site and ensuring that sample holding vessels are extremely well sealed against leaks from atmosphere.

The calibrated distribution functions were used as initial conditions to determine water persistence through a TPD simulation program that uses the lunar temperature cycle for various latitudes as its temperature cycle. Similar to a TPD in the lab, it was

assumed that any water that desorbed from the surface was lost and would not readsorb. This program predicts the maximum adsorbed water that would be stable against thermal desorption only and does not account for radiation or impact effects. The result is that more water persists on 72501 than on the surrogates, and essentially no water persists on sample 12001. This is because 72501 exhibited the highest desorption activation energies and greatest concentration of chemisorption sites on its surface. The net result of the water persistence simulation is that if water is present on the lunar surface, the direct interaction between the adsorbed water molecule and the soil grain surface is strong enough to hold at least a few ppm of water through an entire lunar day at high latitudes (possibly tens of ppm if greater sticking during the experiment is assumed). However, in a full model, non-thermal loss terms would reduce water retention and must be considered - along with migration, readsorption, and water formation in situ.

The TPD experiments described above represent a significant step forward for understanding the thermal behavior of water adsorbed to lunar materials. However, the number of samples examined is small, and more samples should be examined to improve the understanding to the next level. The allocation of samples received contained five total lunar soils of varying mineralogical composition and mode, maturity index, and possibility of contamination by human activities. The remaining three samples should be analyzed as soon as possible to better understand how diverse the behavior really is. Based on the three variables mentioned above, it is likely that the two lunar samples evaluated thus far are end-members of the range of water adsorption

ability on pristine lunar samples. Each increase in understanding of the thermal behavior of water on lunar materials increases understanding of data returned by spacecraft-based investigations and the sources, evolution, and eventual fate of water on Earth's moon.

Additional, and much needed, perspective regarding water behavior on the Moon will be provided by experiments in the new system being constructed (see Chapter 4) to simulate space weathering processes from the solar wind on lunar-relevant materials, including lunar rock surface cuts. The ability to simultaneously irradiate with two particle sources, while controlling the temperature of the sample *and* monitoring the process *in situ* with infrared spectroscopy and a quadrapole mass spectrometer is unparalleled in the community (to our knowledge). The highest-priority investigations should be examining as-of-yet untested mechanisms for water formation from reaction of solar wind H^+ with regolith oxygen, and examining the effects of active irradiation and defect production on the adsorption and dissociation of water. Both of these investigations are essential to understanding data returned by spacecraft-based investigations and the sources, evolution, and eventual fate of water on Earth's moon.

Finally, investigations of the mechanism of water photolysis on zirconia nanoparticles were carried out to increase understanding of the fundamental process of water decomposition on metal-oxide photocatalysts (see Chapter 5). The photolysis was found to occur by a multi-step process of photon absorption in the zirconia nanoparticles followed by exciton migration and energy transfer to the adsorbed water molecule. The difference in hydrogen yield between the monoclinic and cubic phase

nanoparticles was found to be a result of exciton recombination at crystal defects, preventing excitons from reaching the water molecules at the surface or transferring their energy to them, in the cubic phase nanoparticles. Coverage-dependent examination of hydrogen production showed that photo-induced water-splitting is primarily a surface-mediated event and the use of nanoparticles is generally beneficial due to enhanced surface-to-volume ratios. Future examinations on this system could include detailed investigation of the nature of the adsorbed water by diffuse reflectance infrared spectroscopy, ultraviolet and x-ray photoemission spectroscopy, and temperature programmed desorption. Knowledge of the nature of interaction between the surface and the adsorbed water may produce insights into the engineering of future catalysts for water photolysis with lower energy photons.

References

Arakawa, H., and K. Sayama (2000), Solar hydrogen production. Significant effect of Na_2CO_3 addition on water splitting using simple oxide semiconductor photocatalysts, *Catal. Surv. Jpn.*, *4*(1), 75-80.

Arnold, J. R. (1979), Ice in the Lunar Polar Regions, *Journal of Geophysical Research*, *84*(NB10), 5659-5668.

Band, Y. B. (2006), *Light and Matter*, John Wiley and Sons Inc., Chichester.

Barrie, P. J. (2008), Analysis of temperature programmed desorption (tpd) data for the characterization of catalysts containing a distribution of adsorption sites, *Phys. Chem. Chem. Phys.*, *10*(12), 1688-1696, doi: 10.1039/b717430f.

Bennett, C. J., C. Pirim, and T. M. Orlando (2013), Space-Weathering of Solar System Bodies: A Laboratory Perspective, *Chemical Reviews*, *113*(12), 9086-+, doi:10.1021/cr400153k.

Bondioli, F., A. M. Ferrari, C. Leonelli, C. Siligardi, and G. C. Pellacani (2001), Microwave-hydrothermal synthesis of nanocrystalline zirconia powders, *J. Am. Ceram. Soc.*, *84*(11), 2728-2730.

Boyce, J. W., Y. Liu, G. R. Rossman, Y. B. Guan, J. M. Eiler, E. M. Stolper, and L. A. Taylor (2010), Lunar apatite with terrestrial volatile abundances, *Nature*, *466*(7305), 466-U462, doi: 10.1038/nature09274.

Bradley, J. P., H. A. Ishii, J. J. Gillis-Davis, J. Ciston, M. H. Nielsen, H. A. Bechtel, and M. C. Martin (2014), Detection of solar wind-produced water in irradiated rims on silicate minerals, *Proceedings of the National Academy of Sciences of the United States of America*, *111*(5), 1732-1735, doi:10.1073/pnas.1320115111.

Brunauer, S., P. H. Emmett, and E. Teller (1938), Adsorption of gases in multimolecular layers, *JACS*, *60*, 309-319.

Burke, D. J., C. A. Dukes, J. H. Kim, J. Shi, M. Fama, and R. A. Baragiola (2011), Solar wind contribution to surficial lunar water: Laboratory investigations, *Icarus*, *211*(2), 1082-1088, doi: 10.1016/j.icarus.2010.11.007.

Cadenhead, D. A., M. G. Brown, D. K. Rice, and J. R. Stetter (1977), Some surface area and porosity characterizations of lunar soils, *Proc. Lunar Planet. Sci. Conf 8th*, 1291.

Chang, S. M., and R. A. Doong (2005), Chemical-composition-dependent metastability of tetragonal ZrO_2 in sol-gel-derived films under different calcination conditions, *Chemistry of Materials*, *17*(19), 4837-4844, doi:10.1021/cm051264t.

Ciuparu, D., A. Ensuque, G. Shafeev, and F. Bozon-Verduraz (2000), Synthesis and apparent bandgap of nanophase zirconia, *J. Mater. Sci. Lett.*, *19*(11), 931-933.

Clark, R. N. (2009), Detection of Adsorbed Water and Hydroxyl on the Moon, *Science*, *326*(5952), 562-564, doi:10.1126/science.1178105.

Colaprete, A., et al. (2010), Detection of Water in the LCROSS Ejecta Plume, *Science*, *330*(6003), 463-468, doi:10.1126/science.1186986.

Crider, D. H., and R. R. Vondrak (2000), The solar wind as a possible source of lunar polar hydrogen deposits, *J. Geophys. Res.-Planets*, *105*(E11), 26773-26782.

D'Souza, A. S., and C. G. Pantano (2002), Hydroxylation and dehydroxylation behavior of silica glass fracture surfaces, *J. Am. Ceram. Soc.*, *85*(6), 1499-1504.

Dawley, M. M. (2013), Radiation and thermal processing of ices and surfaces relevant to prebiotic chemistry in the solar system and interstellar regions, Georgia Institute of Technology.

De Jong, A. M., J. W. Niemantsverdriet, (1990), Thermal desorption analysis: comparative test of ten commonly applied procedures, *Surf. Sci., 233*, 355-365.

De Leeuw, N. H., S. C. Parker, C. R. A. Catlow, and G. D. Price (2000), Modeling the effect of water on the surface structure and stability of forsterite, *Phys. Chem. Miner., 27,* 332-341.

De Leeuw, N. H. (2001), Density functional theory calculations of hydrogen-containing defects in forsterite, periclase, and alpha-quartz. *J. Phys. Chem. B 105(40),* 9747-9754

Dohnálek, Z., G. A. Kimmel, S. A. Joyce, P. Ayotte, R. S. Smith, and B. D. Kay (2001), Physisorption of CO on the MgO(100) Surface, *J. Phys. Chem. B, 105,* 3747-3751.

Dyar, M. D., C. A. Hibbitts, and T. M. Orlando (2010), Mechanisms for incorporation of hydrogen in and on terrestrial planetary surfaces, *Icarus*, *208*(1), 425-437, doi: 10.1016/j.icarus.2010.02.014.

Epstein, S., and H. P. Taylor, Jr. (1974), Deuterium/hydrogen and oxygen-18/oxygen-16 ratios of water in the rusty breccia 66095 and the origin of lunar water, *Proc. Lunar Sci. Conf.*, *2*, 1839-1854.

French, R., S. Glass, F. Ohuchi, Y.-N. Xu, and W. Ching (1994), Experimental and theoretical determination of the electronic structure and optical properties of three phases of ZrO_2, *Phys. Rev. B*, *49*(8), 5133.

Garcia, J. C., L. M. R. Scolfaro, A. T. Lino, V. N. Freire, G. A. Farias, C. C. Silva, H. W. L. Alves, S. C. P. Rodrigues, and E. F. da Silva (2006), Structural, electronic, and optical properties of ZrO_2 from ab initio calculations, *J. Appl. Phys.*, *100*(10), doi:10.1063/1.2386967.

Gibson, E. K., and S. M. Johnson (1971), Thermal analysis-inorganic gas release studies of lunar samples, *Proc. Lunar Sci. Conf.*, *2*, 1351-1366.

Goering, J., Sah, S., Burghaus, U., Street Jr, K.W., 2008. Adsorption of water on JSC-1A (simulated moon dust samples) – a surface science study. *Surf. Interface Anal. 40*, 1423-1429.

Goumans, T. P. M., C. R. A. Catlow, W. A. Brown, J. Kastner, and P. Sherwood (2009), An embedded cluster study of the formation of water on interstellar dust grains, *Phys. Chem. Chem. Phys.*, 11, 5431-5436, doi: 10.1039/b816905e.

Gladstone, G. R., et al. (2010), LRO-LAMP Observations of the LCROSS Impact Plume, *Science*, *330*(6003), 472-476, doi:10.1126/science.1186474.

Greenwood, J. P., S. Itoh, N. Sakamoto, P. Warren, L. Taylor, and H. Yurimoto (2011a), Hydrogen isotope ratios in lunar rocks indicate delivery of cometary water to the Moon, *Nat. Geosci.*, *4*(2), 79-82, doi:10.1038/ngeo1050.

Greenwood, J. P., S. Itoh, N. Sakamoto, P. H. Warren, M. D. Dyar, and H. Yurimoto (2011b), Origin of Lunar Water and Evidence for a Wet Moon from D/H and Water in Lunar Apatites, *Lunar Planet. Sci.*, *41st*, Abstract 2753.

Grieves, G., C. A. Hibbitts, M. D. Dyar, T. M. Orlando, M. Poston, and A. Johnson (2010), Mobility and Subsurface Redistribution of Volatiles through Regolith Materials, *Lunar Planet. Sci.*, *41st*, Abstract 2552.

Han, M. (2008), Development of Synthesis Method for Spinel Ferrite Magnetic Nanoparticle and Its Superparamagnetic Properties, Georgia Institute of Technology, Atlanta.

Harmon, J. K., and M. A. Slade (1992), Radar mapping of Mercury - full-disk images and polar anomalies, *Science*, *258*(5082), 640-643, doi:10.1126/science.258.5082.640.

Heiken, G., D. Vaniman, and B. M. French (1991), *Lunar Sourcebook: A User's Guide to the Moon*, Cambridge University Press.

Henderson, M. A. (2002), The interaction of water with solid surfaces: Fundamental aspects revisited, *Surf. Sci. Rep.*, *46*, 5-308, doi: 10.1016/S0167-5729(01)00020-6.

Hendrix, A. R., et al. (2012), The lunar far-UV albedo: Indicator of hydration and weathering, *J. Geophys. Res.*, *117*, E12001, doi:10.1029/2012JE004252.

Hibbitts, C. A., M. D. Dyar, T. M. Orlando, G. Grieves, D. Moriarty, M. Poston, and A. Johnson (2010), Thermal stability of water and hydroxyl on airless bodies, *Lunar Planet. Sci.*, *41st*, Abstract 2417.

Hibbitts, C. A., G. A. Grieves, M. J. Poston, M. D. Dyar, A. B. Alexandrov, M. A. Johnson, and T. M. Orlando (2011), Thermal stability of water and hydroxyl on the surface of the Moon from temperature-programmed desorption measurements of lunar analog materials, *Icarus*, *213*(1), 64-72, doi: 10.1016/j.icarus.2011.02.015.

Hodges, R. R. (2002), Ice in the lunar polar regions revisited, *J. Geophys. Res.-Planets*, *107*(E2), 7, 5011, doi: 10.1029/2000je001491.

Holmes, H. F., E. L. Fuller, and R. A. Beh (1974), Adsorption of Argon, Nitrogen, and Water-Vapor on Zirconium Oxide, *J. Colloid Interface Sci.*, *47*(2), 365-371.

Housley, R. M., E. H. Cirlin, N. E. Paton, and I. B. Goldberg (1974), Solar wind micrometeorite alteration of the lunar regolith, *Proc. Lunar Planet. Sci. Conf 5th*, *3*, 2623.

Hurley, D. (2010), Surficial OH/H_2O on the moon: Modeling delivery, resistribution, and loss, *Lunar Planet. Sci.*, *41st*, Abstract 1844.

Hui, H. J., A. H. Peslier, Y. X. Zhang, and C. R. Neal (2013), Water in lunar anorthosites and evidence for a wet early Moon, *Nat. Geosci.*, *6*(3), 177-180, doi:10.1038/ngeo1735.

Ichimura, A. S., A. P. Zent, R. C. Quinn, and L. A. Taylor (2011), Formation and detection of OH/OD in lunar soils after $^1H_2^+/D_2^+$ bombardment, *Lunar Planet. Sci.*, *42nd*, Abstract 2724.

Ichimura, A. S., A. P. Zent, R. C. Quinn, M. R. Sanchez, and L. A. Taylor (2012), Hydroxyl (OH) production on airless planetary bodies: Evidence from H^+/D^+ ion-beam experiments, *Earth Planet. Sci. Lett.*, *345*, 90-94, doi:10.1016/j.epsl.2012.06.027.

Kimmel, G. A., and T. M. Orlando (1995), Low-Energy (5-120 eV) Electron-Stimulated Dissociation of Amorphouse D_2O Ice - $D(^2S)$, $O(^3P_{2,1,0})$, and $O(^1D_2)$ Yields and Velocity Distributions, *Physical Review Letters*, *75*(13), 2606-2609, doi:10.1103/PhysRevLett.75.2606.

Kralik, B., E. K. Chang, and S. G. Louie (1998), Structural properties and quasiparticle band structure of zirconia, *Phys. Rev. B*, *57*(12), 7027-7036, doi:10.1103/PhysRevB.57.7027.

Kolasinski, K. W. (2002), Surface Science: Foundations of Catalysis and Nanoscience, John Wiley, New York.

Kudo, A., and Y. Miseki (2009), Heterogeneous photocatalyst materials for water splitting, *Chemical Society Reviews*, *38*(1), 253-278, doi:10.1039/b800489g.

LaVerne, J. A. (2005), H_2 formation from the radiolysis of liquid water with zirconia, *Journal of Physical Chemistry B*, *109*(12), 5395-5397.

Lawrence, D. J., W. C. Feldman, R. C. Elphic, J. J. Hagerty, S. Maurice, G. W. McKinney, and T. H. Prettyman (2006), Improved modeling of Lunar Prospector neutron spectrometer data: Implications for hydrogen deposits at the lunar poles, *Journal of Geophysical Research*, *111*, E08001.

Lawrence, D. J., D. M. Hurley, W. C. Feldman, R. C. Elphic, S. Maurice, R. S. Miller, and T. H. Prettyman (2011), Sensitivity of orbital neutron measurements to the thickness and abundance of surficial lunar water, *J. Geophys. Res.-Planets*, *116*, 13, E01002, doi: 10.1029/2010je003678.

Lawrence, D. J., et al. (2013), Evidence for Water Ice Near Mercury's North Pole from MESSENGER Neutron Spectrometer Measurements, *Science*, *339*(6117), 292-296, doi:10.1126/science.1229953.

Leich, D. A., Tombrell.Ta, and D. S. Burnett (1973), Depth distribution of hydrogen in lunar materials, *Earth Planet. Sci. Lett.*, *19*(3), 305-314, doi:10.1016/0012-821x(73)90080-0.

Liu, Y., Y. B. Guan, Y. X. Zhang, G. R. Rossman, J. M. Eiler, and L. A. Taylor (2012), Direct measurement of hydroxyl in the lunar regolith and the origin of lunar surface water, *Nat. Geosci.*, *5*(11), 779-782, doi:10.1038/ngeo1601.

Livengood, T. A., G. Chin, R. Sagdeev, I. G. Mitrofanov, W. V. Boynton, L. G. Evans, M. L. Litvak, T. P. McClanahan, A. B. Sanin, and R. D. Starr (2014), Evidence for diurnally varying hydration at the Moon's equator from the lunar exploration neutron detector (LEND), *Lunar Planet. Sci.*(45th), 1507.

Lucey, P., R. L. Korotev, J. J. Gillis, L. A. Taylor, D. Lawrence, B. A. Campbell, R. Elphic, B. Feldman, L. L. Hood, D. Hunten, M. Mendillo, S. Noble, J. J. Papike, R. C. Reedy, S. Lawson, T. Prettyman, O. Gasnault, and S. Maurice (2006), Understanding the lunar surface and space-moon interactions, in *New views of the moon*, edited, pp. 83-+, Mineralogical Soc America, Chantilly.

Lucey, P. G. (2009), A lunar water world, *Science*, *326*(5952), 531-532, doi: 10.1126/science.1181471.

Managadze, G. G., V. T. Cherepin, Y. G. Shkuratov, V. N. Kolesnik, and A. E. Chumikov (2011), Simulating OH/H_2O formation by solar wind at the lunar surface, *Icarus*, *215*(1), 449-451, doi:10.1016/j.icarus.2011.06.025.

McCord, T. B., L. A. Taylor, J. P. Combe, G. Kramer, C. M. Pieters, J. M. Sunshine, and R. N. Clark (2011), Sources and physical processes responsible for OH/H_2O in the lunar soil as revealed by the moon mineralogy mapper (m-3), *J. Geophys. Res.-Planets*, *116*, 22, E00g05, doi: 10.1029/2010je003711.

McKay, D. S., J. L. Carter, W. W. Boles, C. C. Allen, and J. H. Allton (1994), JSC-1: A new lunar soil simulant, *Engineering, Construction, and Operations in Space IV*, American Society of Civil Engineers, pp. 857-866.

Mitrofanov, I. G. e. a. (2010), Hydrogen Mapping of the Lunar South Pole Using the LRO Neutron Detector Experiment LEND, *Science*, *330*, 483.

Morris, R. V. (1978), The surface exposure (maturity) of lunar soils: Some concepts and I_S/FeO compilation, *Proc. Lunar Planet. Sci. Conf 9th*, 2287.

Navio, J. A., M. C. Hidalgo, G. Colon, S. G. Botta, and M. I. Litter (2001), Preparation and physicochemical properties of ZrO_2 and Fe/ZrO_2 prepared by a sol-gel technique, *Langmuir*, *17*(1), 202-210.

Neugebauer, M., and C. W. Snyder (1962), Solar Plasma Experiment, *Science*, *138*(3545), 1095-1097, doi:10.2307/1709487.

Neumann, G. A., et al. (2013), Bright and Dark Polar Deposits on Mercury: Evidence for Surface Volatiles, *Science*, *339*(6117), 296-300, doi:10.1126/science.1229764.

Ong, L., E. I. Asphaug, D. Korycansky, and R. F. Coker (2010), Volatile retention from cometary impacts on the Moon, *Icarus*, *207*(2), 578-589, doi: 10.1016/j.icarus.2009.12.012.

Orlando, T.M., A. B. Aleksandrov, J. Herring (2003), Electron-Stimulated Desorption of H+, H2+, OH+, and H+(H2O)*n* from Water-Covered Zirconia Surfaces, *J. Phys. Chem. B*, 107, 9370-9376, doi: 10.1021/jp030117k.

Paige, D. A. e. a. (2010), Diviner Lunar Radiometer Observations of Cold Traps in the Moon's South Polar Region, *Science*, *330*, 479.

Paige, D. A., M. A. Siegler, J. K. Harmon, G. A. Neumann, E. M. Mazarico, D. E. Smith, M. T. Zuber, E. Harju, M. L. Delitsky, and S. C. Solomon (2013), Thermal Stability of

Volatiles in the North Polar Region of Mercury, *Science*, *339*(6117), 300-303, doi:10.1126/science.1231106.

Petrik, N. G., A. B. Alexandrov, and A. I. Vall (2001), Interfacial energy transfer during gamma radiolysis of water on the surface of ZrO_2 and some other oxides, *Journal of Physical Chemistry B*, *105*(25), 5935-5944, doi:10.1021/jp004440o.

Petrunin, V. F., V. V. Popov, H. Z. Zhu, and A. A. Timofeev (2004), Synthesis of nanocrystalline high-temperature zirconia phases, *Inorg. Mater.*, *40*(3), 251-258, doi:10.1023/b:inma.0000020523.89340.46.

Pieters, C. M., J. N. Goswami, R. N. Clark, M. Annadurai, J. Boardman, B. Buratti, J. P. Combe, M. D. Dyar, R. Green, J. W. Head, C. Hibbitts, M. Hicks, P. Isaacson, R. Klima, G. Kramer, S. Kumar, E. Livo, S. Lundeen, E. Malaret, T. McCord, J. Mustard, J. Nettles, N. Petro, C. Runyon, M. Staid, J. Sunshine, L. A. Taylor, S. Tompkins, and P. Varanasi (2009), Character and spatial distribution of OH/H_2O on the surface of the moon seen by m-3 on chandrayaan-1, *Science*, *326*(5952), 568-572, doi: 10.1126/science.1178658.

Poston, M. J., G. A. Grieves, A. B. Aleksandrov, C. A. Hibbitts, M. D. Dyar, and T. M. Orlando (2013), Water interactions with micronized lunar surrogates JSC-1A and albite under ultra-high vacuum with application to lunar observations, *J. Geophys. Res.-Planets*, *118*(1), doi:10.1029/2012je004283.

Reddy, V. R., D. W. Hwang, and J. S. Lee (2003), Photocatalytic water splitting over ZrO_2 prepared by precipitation method, *Korean J. Chem. Eng.*, *20*(6), 1026-1029, doi:10.1007/bf02706932.

Robens, E., A. Bischoff, A. Schreiber, A. Dabrowski, and K. K. Unger (2007), Investigation of surface properties of lunar regolith: Part i, *Appl. Surf. Sci.*, *253*(13), 5709-5714.

Roth, O., B. Dhalgren, and J. A. LaVerne (2012), Radiolysis of Water on ZrO_2 Nanoparticles, *Journal of Physical Chemistry C*, *116*, 17619-17624, doi:dx.doi.org/10.1021/jp304237c.

Saal, A. E., E. H. Hauri, M. Lo Cascio, J. A. Van Orman, M. C. Rutherford, and R. F. Cooper (2008), Volatile content of lunar volcanic glasses and the presence of water in the Moon's interior, *Nature*, *454*(7201), 192-U138, doi:10.1038/nature07047.

Sayama, K., and H. Arakawa (1993), Photocatalytic Decomposition of Water and Photocatalytic Reduction of Carbon-Dioxide over ZrO_2 Catalyst, *J. Phys. Chem.*, *97*(3), 531-533.

Sayama, K., and H. Arakawa (1994), Effect of Na_2CO_3 Addition on Photocatalytic Decomposition of Liquid Water over various Semoiconductor Catalysts, *Journal of Photochemistry and Photobiology a-Chemistry*, *77*(2-3), 243-247.

Sayama, K., and H. Arakawa (1996), Effect of carbonate addition on the photocatalytic decomposition of liquid water over a ZrO_2 catalyst, *Journal of Photochemistry and Photobiology a-Chemistry*, *94*(1), 67-76.

Siegler, M. A., B. G. Bills, and D. A. Paige (2011), Effects of orbital evolution on lunar ice stability, *J. Geophys. Res.-Planets*, *116*, 18, doi: E03010, 10.1029/2010je003652.

Sunshine, J. M., T. L. Farnham, L. M. Feaga, O. Groussin, F. Merlin, R. E. Milliken, and M. F. A'Hearn (2009), Temporal and spatial variability of lunar hydration as observed by the deep impact spacecraft, *Science*, *326*(5952), 565-568, doi: 10.1126/science.1179788.

Taylor, L. A., G. R. Rossman, and Q. Qi (1995), Where has all the lunar water gone?, *Abstracts of the Lunar and Planetary Science Conference* , 26, 1399-1400.

Taylor, M. A., R. E. Alonso, L. A. Errico, A. Lopez-Garcia, P. de la Presa, A. Svane, and N. E. Christensen (2012), Structural, electronic, and hyperfine properties of pure and Ta-doped m-ZrO_2, *Phys. Rev. B*, *85*(15), doi:10.1103/PhysRevB.85.155202.

Thiel, P. A., and T. E. Madey (1987), The interaction of water with solid-surfaces - fundamental aspects, *Surf. Sci. Rep.*, *7*(6-8), 211-385.

van de Krol, R., Y. Q. Liang, and J. Schoonman (2008), Solar hydrogen production with nanostructured metal oxides, *J. Mater. Chem.*, *18*(20), 2311-2320, doi:10.1039/b718969a.

Vasavada, A. R., D. A. Paige, and S. E. Wood (1999), Near-surface temperatures on mercury and the Moon and the stability of polar ice deposits, *Icarus*, *141*(2), 179-193.

Vidali, G., and L. Li (2010), Molecular hydrogen desorption from amorphous surfaces at low temperature, *Journal of Physics-Condensed Matter*, *22*(30), doi:10.1088/0953-8984/22/30/304012.

Wallace, W. T., L. A. Taylor, Y. Liu, B. L. Cooper, D. S. McKay, B. Chen, and A. S. Jeevarajan (2009), Lunar dust and lunar simulant activation and monitoring, *Meteorit. Planet. Sci.,* 44, 961–970, doi:10.1111/j.1945-5100.2009.tb00781.x.

Watson, K., B. C. Murray, and H. Brown (1961), The Behavior of Volatiles on the Lunar Surface, *Journal of Geophysical Research*, *66*(9), 3033.

Yoshimura, M., and S. Somiya (1999), Hydrothermal synthesis of crystallized nano-particles of rare earth-doped zirconia and hafnia, *Mater. Chem. Phys.*, *61*(1), 1-8, doi:10.1016/s0254-0584(99)00104-2.

Yuan, Y. P., X. L. Zhang, L. F. Liu, X. J. Jiang, J. Lv, Z. S. Li, and Z. G. Zou (2008), Synthesis and photocatalytic characterization of a new photocatalyst $BaZrO_3$, *Int. J. Hydrogen Energ.*, *33*(21), 5941-5946, doi:10.1016/j.ijhydene.2008.07.052.

Zhang, Y., V. Ji, and K. W. Xu (2013), The detailed geometrical and electronic structures of monoclinic zirconia, *J. Phys. Chem. Solids*, *74*(3), 518-523, doi:10.1016/j.jpcs.2012.11.021.

Zeller, E. J., L. B. Ronca, and P. W. Levy (1966), Proton-induced hydroxyl formation on lunar surface, *Journal of Geophysical Research*, *71*(20), 4855.